Understanding Heavy Lake-Effect Snowfall: The Vertical Structure of Radar Reflectivity in a Deep Snowband over and downwind of Lake Ontario

DAN WELSH, BART GEERTS, XIAOQIN JING, AND PHILIP T. BERGMAIER

Department of Atmospheric Science, University of Wyoming, Laramie, Wyoming

JUSTIN R. MINDER

Department of Atmospheric and Environmental Sciences, University at Albany, State University of New York, Albany, New York

W. JAMES STEENBURGH AND LEAH S. CAMPBELL

Department of Atmospheric Sciences, University of Utah, Salt Lake City, Utah

(Manuscript received 17 February 2016, in final form 31 July 2016)

ABSTRACT

The distribution of radar-estimated precipitation from lake-effect snowbands over and downwind of Lake Ontario shows more snowfall in downwind areas than over the lake itself. Here, two nonexclusive processes contributing to this are examined: the collapse of convection that lofts hydrometeors over the lake and allows them to settle downwind; and stratiform ascent over land, due to the development of a stable boundary layer, frictional convergence, and terrain, leading to widespread precipitation there. The main data sources for this study are vertical profiles of radar reflectivity and hydrometeor vertical velocity in a well-defined, deep long-lake-axis-parallel band, observed on 11 December 2013 during the Ontario Winter Lake-effect Systems (OWLeS) project. The profiles are derived from an airborne W-band Doppler radar, as well as an array of four K-band radars, an X-band profiling radar, a scanning X-band radar, and a scanning S-band radar.

The presence of convection offshore is evident from deep, strong (up to 10 m s^{-1}) updrafts producing bounded weak-echo regions and locally heavily rimed snow particles. The decrease of the standard deviation, skewness, and peak values of Doppler vertical velocity during the downwind shore crossing is consistent with the convection collapse hypothesis. Consistent with the stratiform ascent hypothesis are (i) an increase in mean vertical velocity over land; and (ii) an increasing abundance of large snowflakes at low levels and over land, due to depositional growth and aggregation, evident from flight-level and surface particle size distribution data, and from differences in reflectivity values from S-, X-, K-, and W-band radars at nearly the same time and location.

1. Introduction

Lake Ontario and the downstream areas experience lake-effect snowstorms, some of which are capable of producing persistent, heavy snowfall (Eichenlaub 1979; Niziol et al. 1995; Burt 2007; Markowski and Richardson 2010; Steiger et al. 2013; Veals and Steenburgh 2015). Lake-effect snow results from boundary layer convection. This convection may appear cellular, and either disorganized ("broad coverage") or in regularly spaced bands (or "streets") due to the presence of horizontal convective roll circulations (Young et al. 2002). Such cellular convection tends to produce light to moderate snowfall (Niziol et al. 1995; Kristovich and Steve 1995). In some cases, when the boundary layer wind is roughly aligned with the long axis of the lake, a well-defined, continuous band of elevated reflectivity forms. This type of organization, known as a long-lake-axis-parallel (LLAP) band, produces more vigorous yet localized snowfall and is most common over Lakes Erie and Ontario (Jiusto and Kaplan 1972; Niziol et al. 1995; Kristovich and Steve 1995; Steiger et al. 2013; Veals and Steenburgh 2015). LLAP bands result, in part, from a lake-scale secondary circulation with low-level convergence (Peace and Sykes

Corresponding author address: Bart Geerts, Dept. of Atmospheric Science, University of Wyoming, Laramie, WY 82071.
E-mail: geerts@uwyo.edu

DOI: 10.1175/MWR-D-16-0057.1

1966) and upper-level divergence (Kristovich et al. 2016; Bergmaier et al. 2015).

It appears that lake-effect snowfall is heavier downwind of the shoreline (over land) than offshore in most lake-effect systems (LeS), including LLAP events. This distribution is noted particularly near Lake Ontario (Jiusto and Kaplan 1972; Wilson 1977; Minder et al. 2015; Veals and Steenburgh 2015), as was the case for an LLAP event on 11 December 2013. The present study focuses on this particular event, observed intensively as part of the Ontario Winter Lake-effect Systems (OWLeS) project (Kristovich et al. 2016).

The objective of this investigation is to use data collected in the 11 December 2013 OWLeS case [intensive observation period (IOP) 2b], primarily profiling radar data, to identify processes contributing to the observed downwind increase of precipitation from a strong LLAP band. Two complementary hypotheses are explored in this study. An idealized representation of aspects of these hypotheses is shown in Fig. 1. First, it should be noted that the structure of the offshore LLAP band is not uniform. Its low-level convergence, secondary circulation, updraft strength, depth, and precipitation production all grow with fetch from the upwind (western) shore of Lake Ontario. As will be shown later, the LLAP band is most organized and deepest just off the eastern shore of the lake. The two hypotheses are as follows:

1) *Collapse of convection.* This hypothesis states that convective updrafts rapidly weaken as they are advected across the shoreline, for lack of surface heating. Over water, precipitation in convective updrafts will only reach the surface by achieving fall speeds great enough to overcome upward air motions. Houze (2014) separates convective and stratiform precipitation based on vertical air motion: convective updrafts (early in the life cycle of convection) exceed the hydrometeor fall speed ($\sim 1.0\,\mathrm{m\,s^{-1}}$ for unrimed snow) whereas stratiform ascent rates do not. While many precipitation particles will reach the surface over the lake, a substantial fraction will remain suspended for some time in convective updrafts. The collapse of these updrafts over land then allows hydrometeors to readily fall to the surface.

   The convection collapse hypothesis expects strong, localized updrafts with weaker, intermediate downdrafts over the lake, and decreasing updraft strength and organization over land. Accordingly, larger values of standard deviation σ_w and skewness μ_w of vertical velocity w are expected over the lake. Also, the echo-top height is expected to decrease onshore (Fig. 1). This mechanism, by itself, will not change the spatial texture of precipitation (mapped radar reflectivity) from convective to stratiform, and is not expected to increase the size of precipitation particles moving inland of the lake.

2) *Stratiform ascent.* This hypothesis states that snow grows in the lake-modified boundary layer in air saturated by several lifting mechanisms. An obvious mechanism is orographic lift, which is possible east of Lake Ontario on account of the Tug Hill Plateau (the Tug for short). In addition to this, ascent over a shallow cold dome, which forms downwind of the shoreline (Fig. 1) by surface cooling or by advection of cooler air not modified by the lake, aids in layer lifting. Additionally, frictional convergence during the lake-to-land transition and remnants of the cross-band thermally direct circulation over the lake may also aid in ascent over land. A separation of the individual contributions of these processes is impossible, yet in concert these processes cause widespread lifting, referred to collectively as stratiform ascent, leading to low-level clouds over land, and supporting snow growth.

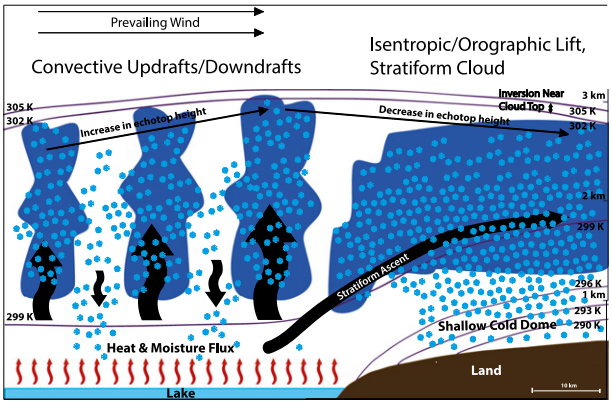

FIG. 1. Schematic representation of processes that take place in landfalling LLAP bands. The solid contours are isentropes.

Expectations arising from the stratiform ascent hypothesis include an increase in mean vertical air velocity, particularly at low levels at close fetch from the shoreline. Updrafts are weak and widespread, implying small values for σ_w and μ_w. An increase in reflectivity in the LLAP band at all levels is anticipated, as is an increase in mean diameter of snow, because layer lifting allows prolonged growth by vapor deposition and aggregation.

These two processes are not mutually exclusive. This study aims to present evidence corroborating (or refuting) each of these processes in one LLAP event observed during OWLeS. It builds on Minder et al. (2015), who use K-band radar reflectivity profiles collected from four sites between the shore and the Tug to show that with increasing inland distance, echoes transition from a

convective toward a stratiform morphology, becoming less intense and more uniform, in IOP2 and in other LeS events during OWLeS.

The next section will describe the instruments and analysis methods used in the study. Section 3 highlights the environmental conditions and LLAP band structure in IOP2b. Section 4 evaluates millimeter-wavelength radar profiles, Section 5 explores hydrometeor characteristics using in situ probes, and section 6 examines differences in millimeter- and centimeter-wavelength radar reflectivity, as an indicator for particle size. The findings are summarized in section 7.

2. Instruments and analysis methods

The full OWLeS experimental design and instrument array are summarized in Kristovich et al. (2016). We only describe instruments and analysis methods used in this case study.

a. *Wyoming Cloud Radar and flight-level particle probes*

The Wyoming Cloud Radar (WCR) is a 95-GHz (3-mm wavelength, W band) pulsed Doppler cloud radar with a beamwidth of 0.5°–0.7°, deployed on board the University of Wyoming King Air (UWKA) research aircraft (Wang et al. 2012). During OWLeS the WCR operated with three fixed antennas: one pointing up (zenith), one down (nadir), and one slant forward. The zenith and nadir antennas yield vertical cross sections of reflectivity Z and Doppler velocity along the flight track, centered at flight level. The Doppler velocity is corrected for aircraft motion when the antenna points off-vertical. Horizontal wind also affects the near-vertical beam, especially when roll or pitch angles are significant. To obtain the best possible estimate of hydrometeor vertical velocity, a nearby OWLeS sounding is used to remove the contribution of the wind in the nadir and zenith antenna Doppler velocities. The WCR range resolution is 30 m during this event, and a representative resolution of independent samples at a range of 1–2 km is about $30 \times 30\,m^2$ (Geerts et al. 2006). The combination of the nadir and slant forward antennas allows dual-Doppler synthesis in vertical transects below flight level. This capability is not used here, but we refer to Bergmaier et al. (2015) for dual-Doppler flow analyses for this case.

Particle size distributions are measured on board the UWKA by two optical array probes, each sorting particles into 101 bins of equal width: a Cloud Imaging Probe (CIP sizing 0.01–2.51 mm, 25-μm bin width) and a 2D-precipitation probe (2D-P, sizing 0.1–20.1 mm, 200-μm bin width). CIP's first two size bins are ignored because they lack reliability, thus the minimum size used here is 0.06 mm. The size of snow particles is complex; particle probe sizes mentioned in this study refer to the maximum dimension. In situ liquid water content (LWC) is estimated by several probes on the UWKA.

b. *Micro Rain Radars*

A network of four Micro Rain Radars (MRRs) was deployed along a quasi-linear array from the shore to the Tug, in the vicinity of the climatologically highest frequency of LLAP band occurrence (Veals and Steenburgh 2015) (Fig. 2). The Sandy Beach (SB) site is on the eastern lakeshore, while the upper plateau (UP) site is ~40 km inland and 470 m higher in elevation (Table 1). The MRRs are frequency-modulated continuous wave Doppler radars, with a transmit frequency of 24 GHz (1.24-cm wavelength, K band) and a beamwidth of 2° (Klugmann et al. 1996). The range resolution of the MRRs is 200 m in OWLeS. Reflectivity calibration and data processing of the MRR array in OWLeS is discussed by Minder et al. (2015) and Maahn and Kollias (2012).

c. *Mobile Integrated Profiling System*

The University of Alabama Huntsville's Mobile Integrated Profiling System (MIPS) was deployed near the MRR at the Sandy Creek (SC) site (Fig. 2). The MIPS array includes the X-Band Profiling Radar (XPR), a zenith-pointing passive microwave profiling radiometer (MPR), and a PARSIVEL disdrometer, among other probes.

The XPR is a vertically pointing, horizontally polarized pulsed radar with a transmit frequency of 9.4 GHz (~3-cm wavelength, X band), a range gate spacing of 50 m, a pulse repetition frequency (PRF) of 1–2 kHz, and a beamwidth of 1.2° (Phillips 2009). The MIPS MPR is a 12-channel radiometer providing vertical profiles of temperature and water vapor (Ware et al. 2003). Through the measurement of passive microwave radiances at various frequencies, a profile of cloud LWC is also derived (Ware et al. 2003). The MPR vertical resolution is inherently limited, and is best (~100 m) near the surface. A Particle Size Velocity (PARSIVEL) disdrometer is an optical sensor with laser diode; it measures particle concentration as a function of size and as a function of fall velocity. The instrument measures the maximum particle diameter in one dimension, which may be smaller than the 3D maximum diameter (Yuter et al. 2006). The diameters are sorted in 32 bins, ranging between 0.062 and 24.5 mm. The lower two size bins are ignored because they lack reliability (Yuter et al. 2006), thus the minimum size is 0.31 mm.

d. *Doppler on Wheels*

The Center for Severe Weather Research (http://www.cswr.org) Doppler on Wheels (DOW) 7 was deployed at

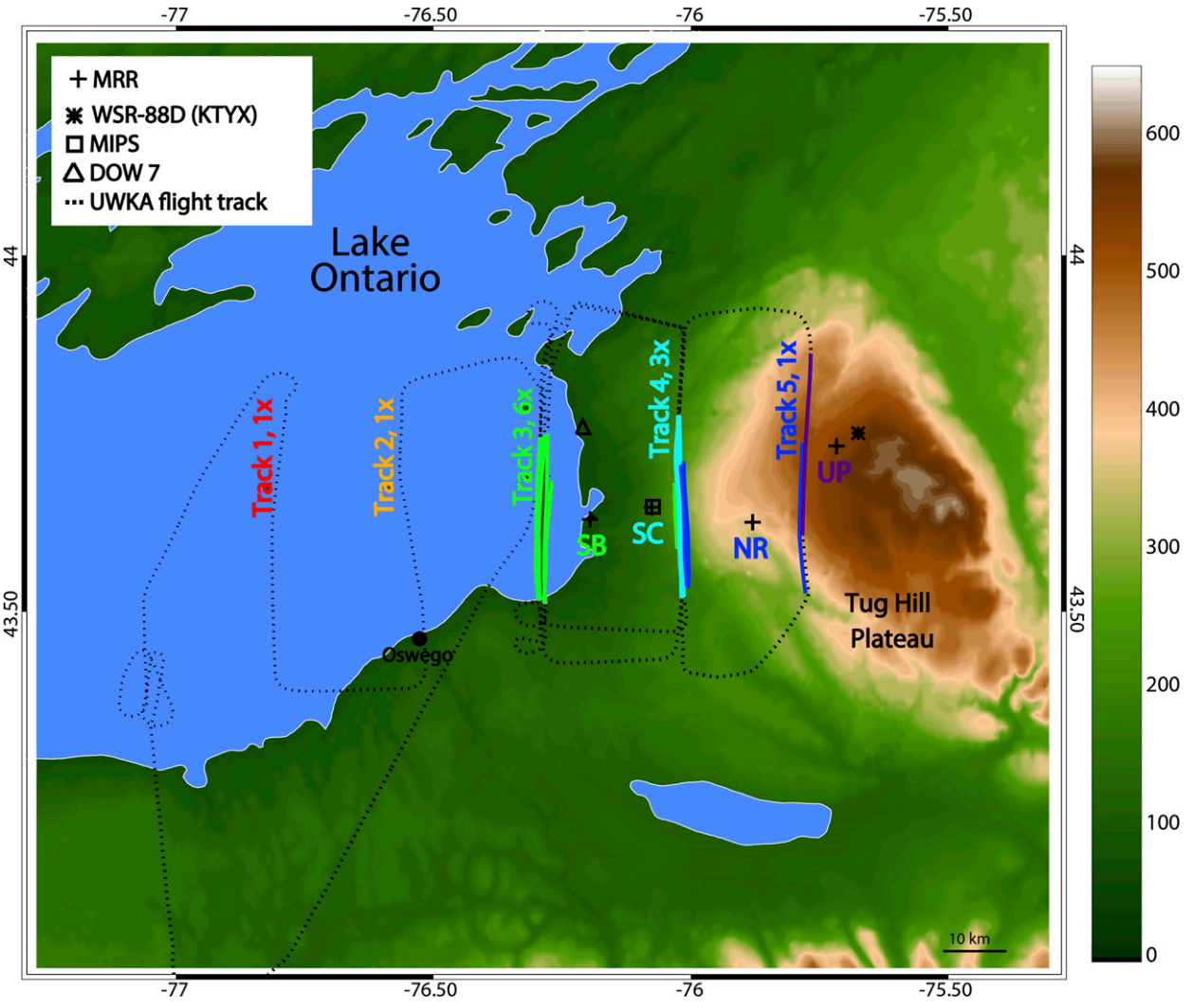

FIG. 2. Terrain map near eastern Lake Ontario including the UWKA flight track on 11 Dec 2013, and instrument sites. Tracks defined by the meridional flight legs are identified, along with the number of passes over each track. Solid flight track sections are within 15 km of MRR sites. The color code identifying specific tracks will be used later in the paper.

Southwick Beach on the eastern end of Lake Ontario (Fig. 2). The DOW is a 9.35/9.50-GHz (~3-cm wavelength, X band) scanning dual-polarization, dual-frequency radar with a beamwidth of 0.93°.

At low-elevation scans, the return power at many DOW radar gates is suspect because of ground clutter, contamination from radar side lobes, anomalous propagation of the radar beam, and other interferences with the underlying surface. Removal of ground clutter is performed using a fuzzy logic algorithm based on the density function for snow and ground clutter (Gourley et al. 2007). Most echoes over water within a 5-km range are removed by this algorithm. The DOW spherical coordinate data (range, azimuth, and elevation) then are interpolated onto a Cartesian grid using a fine vertical resolution and a rather coarse horizontal resolution, since Z profiles are of primary interest. Specifically, a resolution of (1000, 1000, 100) m in the zonal, meridional, and vertical directions is employed, using a Cressman weighting scheme with radii of influence (1000, 1000, 200) m within 20-km range, and (1000, 1000, 400) m outside of this range. More details of the DOW data processing can be found in Jing et al. (2015).

e. *NEXRAD (KTYX)*

Observations from a Next-Generation Radar (NEXRAD, or WSR-88D) located near the top of the Tug (Fig. 2) in Montague, New York (KTYX), are also used in this comparison. KTYX is a 2.8–3.0-GHz (~10.7-cm wavelength, S band) radially scanning dual-polarization

TABLE 1. Snow water equivalent (SWE) accumulation as observed by NCEP stage IV, automated observations, and manual measurements at sites inland of Lake Ontario, covering various time periods on 11 Dec 2013. The nearest grid point is used for the NCEP stage-IV 4-km resolution gridded data. In the first column (+1) refers to the next day (12 Dec 2013). The last column shows the ratio between two sites. Sandy Beach (SB), Sandy Creek (SC), North Redfield (NR), and Upper Plateau (UP).

		SB	SC	NR	UP	
Distance from shore (km)		0.1	9.9	25.5	40.2	
Elev above lake (m)		10	89	312	470	
Time period (UTC)	Source	Cumulative precipitation (mm)				NR/SC
1900–2100	NCEP stage IV	3.00	3.00	3.38	3.88	1.1
	Automated	—	7.61	6.34	—	0.8
1200–1800	NCEP stage IV	3.50	2.00	5.40	5.30	2.7
	Automated	—	2.01	8.03	—	4.0
	Manual	—	4.00	11.50	—	2.9
1800–0000 (+1)	NCEP stage IV	6.40	7.40	11.40	10.40	1.5
	Automated	—	14.92	19.99	—	1.3
	Manual	—	16.50	24.00	—	1.5
1200–0000 (+1)	NCEP stage IV	9.90	9.40	16.80	15.70	1.8
	Automated	—	16.93	28.08	—	1.7
	Manual	—	20.50	35.50	—	1.7

Doppler radar with a range gate spacing of 250 m, PRF of ~0.3–1.4 kHz, and a beamwidth of 1.0° (http://www.roc.noaa.gov). The volume coverage pattern in operation at this time (VCP212) has a high density of low-elevation scans: the lowest three elevation angles are 0.48°, 0.88°, and 1.34°. The level-2 spherical coordinate data are interpolated onto a Cartesian grid in the same way as the DOW data; however, the radius of influence R is a continuous function of radar distance d: $R = [\tan(1°) \times d]/2$.

f. Dual-wavelength ratio

The return from distributed scatterers received by a radar operating at wavelength λ primarily depends on the size of the scatterers. As the diameter D grows such that the size parameter ($\alpha \equiv \pi D/\lambda$) exceeds a threshold value, scattering by these particles transitions from the Rayleigh regime to the Mie regime. This threshold is $\alpha \sim 0.8$ for snow aggregates (Matrosov 2007). This transition not only depends on size but also on particle shape [e.g., Fig. 1 in Matrosov (2007)] and density (e.g., Leinonen and Szyrmer 2015). A more rimed particle has a larger effective refractive index and will deviate from Rayleigh scattering starting at smaller sizes. Also, the "diameter" D is an ambiguous quantity for snow particles, and the radar backscatter cross-sectional size may not correspond with size estimates from in situ probes. While typical hydrometeors scatter within the Rayleigh regime for precipitation centimeter-wavelength radars, W-band radiation is scattered in the Mie regime by large hydrometeors. Backscatter increases with the sixth power of particle size in the Rayleigh regime, but is less size dependent in the Mie regime, thus W-band Z becomes incrementally lower compared to centimeter-wavelength Z, as the size distribution shifts toward larger sizes. Coincident measurements at different radar frequencies can yield particle size information. The dual-wavelength ratio (DWR) is defined as the ratio of equivalent reflectivity factors Z (Gaussiat et al. 2003; Matrosov et al. 2005):

$$\mathrm{DWR} = \frac{Z_{\lambda,l}}{Z_{\lambda,s}}, \tag{1}$$

where subscripts λ, l and λ, s refer to long and short wavelengths, respectively. When this ratio is converted into units of dBZ, this ratio can be written as a difference:

$$\mathrm{DWR} = 10\log\left(\frac{Z_{\lambda,l}}{Z_{\lambda,s}}\right) = 10\log(Z_{\lambda,l}) - 10\log(Z_{\lambda,s}). \tag{2}$$

Assuming a threshold value for α of 0.8, then the Rayleigh–Mie transition takes place at a particle size of ~0.8 mm for the WCR. For the MRRs, the XPR and DOW, and KTYX, this transition occurs at an approximate particle size of 3.2, 7.6, and 27 mm, respectively. These threshold sizes will be highlighted in particle size distributions shown below, but it should be noted that the transition is gradual (as hydrometeor sizes are distributed) and is affected by particle shape and density. In general, large values of $\mathrm{DWR_{K,W}}$ (the difference in Z between the K-band MRR and the W-band WCR) indicate many particles larger than ~0.8 mm. Recent scattering modeling (Leinonen and Szyrmer 2015; Tyynelä and Chandrasekar 2014) as well

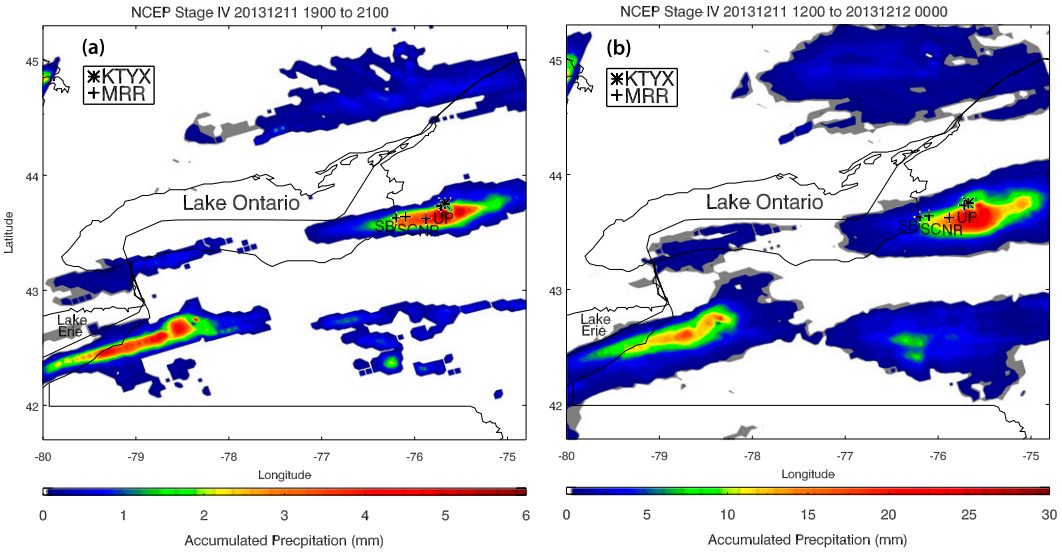

FIG. 3. Map of accumulated precipitation (SWE) for (a) the 2-h period from 1900 to 2100 UTC 11 Dec 2013, and (b) the 12-h period ending at 0000 UTC 12 Dec (NCEP stage-IV data).

as observational studies (Kneifel et al. 2015) have shown that $DWR_{K,W}$ can also be enhanced by relatively small but heavily rimed particles. In fact only if a third radar frequency is available (e.g., X band) can the DWR between two frequency pairs be used to disentangle strongly rimed and largely aggregated particles (Kneifel et al. 2015).

Comparisons drawn here are purely qualitative as the radar illumination volumes are not coincident in time or space, and calibration procedures are different for the various radars.

3. The LLAP band of 11 December 2013

The IOP2b event was one of the more intense, deep, and long-lived LLAP events encountered in OWLeS (Minder et al. 2015; Frame et al. 2015; Campbell et al. 2016). A precipitation maximum [27 mm of snow water equivalent (SWE) in 12 h] occurred on the Tug, about 40 km downwind of the shore of Lake Ontario on 11 December 2013, according to National Centers for Environmental Prediction (NCEP) stage-IV data (Fig. 3). The NCEP stage-IV dataset is a gauge-adjusted NEXRAD reflectivity-based product (Lin and Mitchell 2005), and may be biased because of lack of gauges, the location of the closest NEXRAD radar (KTYX) on a hilltop (the Tug) (Brown et al. 2007), and the shallow nature of lake-effect storms (as will be discussed later). The NCEP stage-IV SWE precipitation amounts are only about half the amounts estimated manually and by gauges at two sites, one at SC (9 km inland, see Fig. 2) and one at North Redfield, New York (NR, 25 km inland), both rather close to the radar (Table 1), suggesting that the Z–R relation is poorly calibrated for this intense LeS event. Manual and gauge measurements and NCEP stage-IV data agree on a 70%–80% increase in snowfall between SC and NR over a 12-h period (Fig. 3b) (Table 1), as described in more detail in Minder et al. (2015) and Campbell et al. (2016). Yet inland (orographic) enhancement is insignificant during the period of interest (1900–2100 UTC), when the LLAP band is best defined, at least between these two sites (Table 1).

This downwind enhancement may be related to lifting caused by low-level stratification and terrain. The presence of the ~600-m-high Tug Hill to the east of Lake Ontario (Fig. 2) likely contributes through orographic influence (Hill 1971; Alcott and Steenburgh 2013; Veals and Steenburgh 2015). This may contribute to the inland increase in the observed precipitation, as the NR site is 223 m higher in elevation than SC. However, a similar pattern of precipitation is seen in the lee of Lake Erie, where the terrain is of lesser influence (Fig. 3), though the downwind enhancement is less pronounced there. This suggests that while orography contributes to snow growth, it is not fully responsible for the observed increase in precipitation from the lakeshore to some distance inland. Isentropic lifting also plays a likely role. The presence of a shallow cold dome during IOP2b is suggested by the difference in virtual potential temperature between SC and NR: over a distance of just 16 km, a ~1.0-K temperature deficit forms in the lowest ~1 km (Fig. 4d). This may be due to the advection of cooler overland air from the

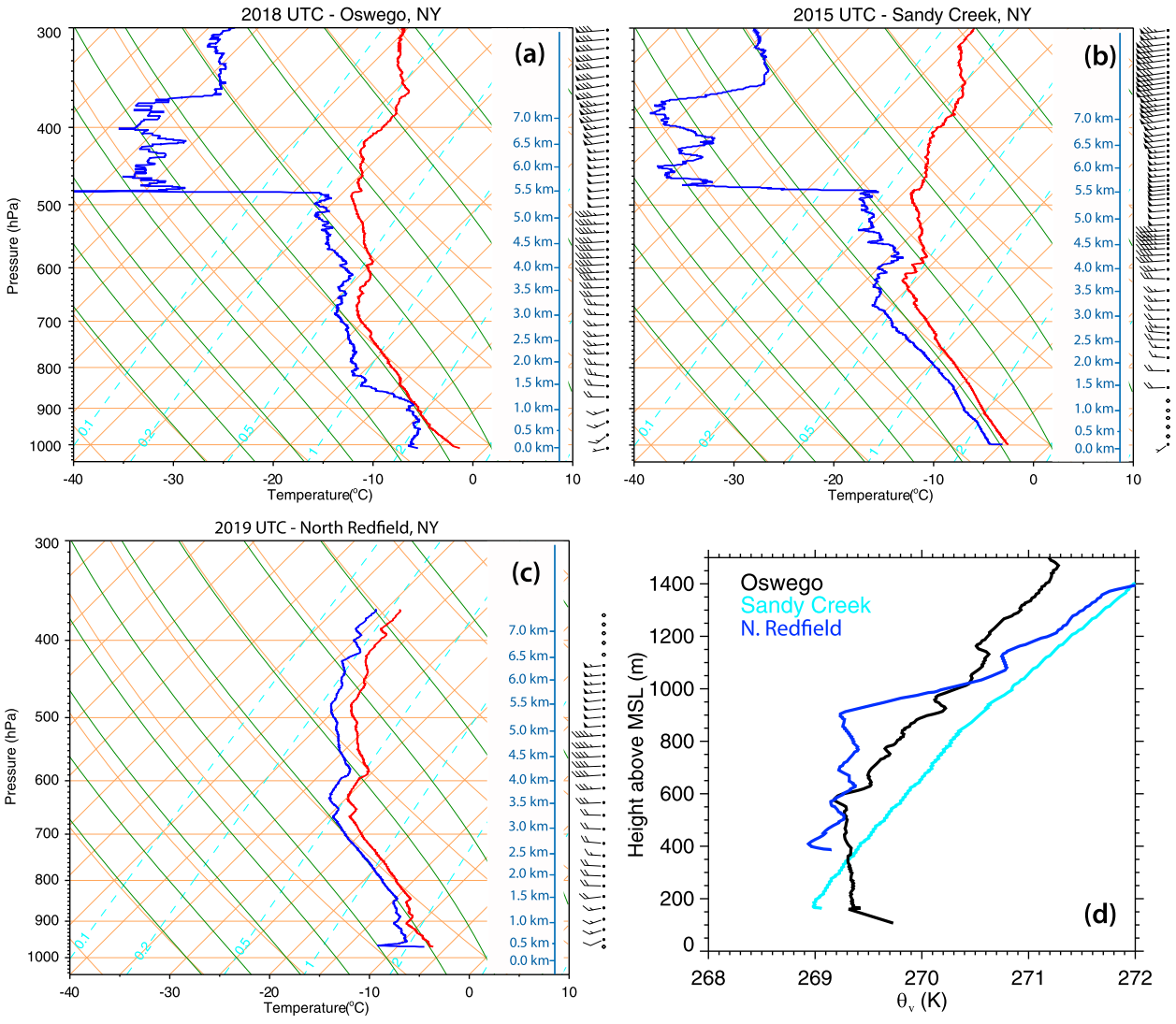

FIG. 4. Data from radiosondes released nearly simultaneously from (a) Oswego, (b) SC, and (c) NR (locations shown in Fig. 2), plotted on a skew T–log$p$ diagram. The wind is plotted on the right of each diagram (long barb = 5 m s^{-1}). (d) Corresponding virtual potential temperature (θ_v) profiles.

southwest (Fig. 2) to NR (Fig. 4c), rather than to surface heat loss between SC and NR. Campbell et al. (2016) show that the relative difference in precipitation amounts (SWE) between the NR and SC sites is larger during this event at times when the LLAP band organization is lesser or absent. This accentuates the role of lifting by these alternate mechanisms in the absence of strong convective forcing.

This research focuses on observations collected between ~1905 and 2105 UTC 11 December 2013, the approximate period that the UWKA research aircraft conducted a series of transects across the LLAP band (Fig. 2). Composite MRR, XPR, DOW, and KTYX data were computed over this period.

This LLAP band formed during an intense cold-air outbreak over Lake Ontario, with 850-hPa temperatures around −16°C, and ~35–40 kt (~18–21 m s^{-1}) wind from the west (Fig. 5). Synoptic conditions are detailed in Campbell et al. (2016). The lake surface waters were still relatively warm (~6°C, not shown) this early in the cold season, resulting in vigorous convection over Lake Ontario. Lake-effect snowfall started the previous day, around 2300 UTC 10 December. Leading up to the period of interest the LeS over Lake Ontario was relatively shallow and disorganized, alternating between organizations featuring a LLAP band and cellular convection covering a broad area of the lake (Campbell et al. 2016). The snowfall rate was also generally less intense during

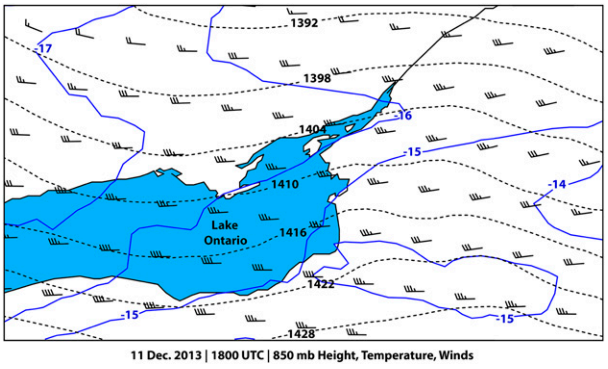

FIG. 5. 850-hPa map of temperature (°C, solid contours), winds (kt, full barb = 10 kt; 1 kt = 0.5144 m s^{-1}), and height (m, dashed contours) over and around eastern Lake Ontario at 1800 UTC 11 Dec (source: 12-km NAM analysis).

this early period compared to the period studied here. The LLAP band studied here became well organized ~1.3 h before the UWKA arrived and remained so until shortly after 2105 UTC (Campbell et al. 2016).

The LLAP band is narrow and highly linear during the period of interest (1905–2105 UTC) (Fig. 6), with rather high echo tops (sometimes exceeding 3 km, Fig. 7) and heavy snowfall downwind (Table 1, Fig. 1). The KTYX base reflectivity map (Fig. 6) indicates that convection is not cellular, but rather linear. The band extends inland over the Tug, KTYX, and farther downwind (Fig. 6).

Several radiosonde soundings were collected during the UWKA flight (Fig. 4): one on the southern lakeshore in Oswego, New York, just beyond the southern edge of the LLAP band, and two more under the band at the SC and NR sites. A deep well-mixed moist layer is present in all soundings, extending up to 3.2 km above mean sea level (MSL) at Oswego (Fig. 2), 3.7 km MSL at SC, and 3.6 km MSL at NR. The capping layer in the SC and NR soundings is particularly stable, consistent with uplift of the base of this layer by upstream LLAP convection. The well-mixed layer is roughly moist adiabatic in all soundings, except for a ~500-m-deep dry-adiabatic layer at Oswego in which water vapor is well mixed. At NR the near-surface air is more humid, implying a lower cloud base, and is slightly more stable at low levels, as previously mentioned.

4. WCR observations

a. WCR transects across the LLAP band

The UWKA flew a "lawnmower pattern" during this event, with 12 cross-LLAP-band flight legs along five geographically fixed meridional tracks (Fig. 2, Table 2). Two of these (tracks 3 and 4) were flown more than once, at different altitudes. The 5 fixed tracks are about 20 km apart: tracks 1–3 are offshore, track 4 is over the coastal plains, and track 5 is over the west side of the Tug Hill Plateau.

Transects along tracks 1–5 (legs 1–5, Table 2), all collected at a flight level of ~3.0 km MSL, are shown in Fig. 7 for Z_{WCR} and in Fig. 8 for WCR-derived hydrometeor vertical velocity w. These transects were flown consecutively (Table 2). They are all ~37 km long, are plotted such that south is on the left in each figure, and are centered on the approximate center of the band as seen from KTYX (the $x = 0$ vertical lines in Figs. 7 and 8 correspond with the location of the dashed line in Fig. 6). Several observations emerge from these transects.

First, the LLAP band is quite deep (~3.0 km) with a Z structure that suggests a secondary circulation with low-level horizontal convergence, an updraft in the middle, and upper-level horizontal divergence. This is particularly noted along tracks 3, 4, and 5 where Z streaks are tilted away from the LLAP band center with height (Figs. 7d,e). This suggests convergence below and divergence aloft. Also, an anvil can be seen in the periphery of the band, with little or no precipitation reaching the ground. This secondary circulation is also suggested by the broad WCR region of ascent near the center of the LLAP band (as seen from KTYX, at $x = 0$), again mainly along the eastern tracks (around $-5 < x < 0$ km in Fig. 8d, $0 < x < 4$ km in Fig. 8e, and more evident in the two later passes along track 4). Along-track horizontal velocities, derived from WCR dual-Doppler data below flight level (using the nadir and slant-forward antennas, section 2a), confirm the presence of a secondary circulation, with low-level confluence of ~10 m s^{-1} across the LLAP band core (Bergmaier et al. 2015; Kristovich et al. 2016). Deep, slow ascent in the center of the LLAP band is not evident along offshore tracks 1–2; perhaps it is overwhelmed by smaller-scale convective up- and downdrafts there.

Second, shallow bounded weak echo regions (BWER) are present within the LLAP band, as illustrated by white arrows in Figs. 7a–d. These regions correspond with updrafts strong enough to evacuate the larger hydrometeors (black arrows in Figs. 8a–d). Convective updrafts are rather shallow along tracks 1 and 2, and are distributed across the band rather than concentrated near the center. A deep, prominent BWER occurs on track 3 (Fig. 7c) on account of a strong updraft, lofting hydrometeors at up to 9.9 m s^{-1} (Fig. 8c). The deepening of the BWERs from track 1 to 3 indicates increasing hydrometeor lofting by convective updrafts. (The highlighted convective updrafts are not the same, as no attempt was made to track these in a Lagrangian sense.)

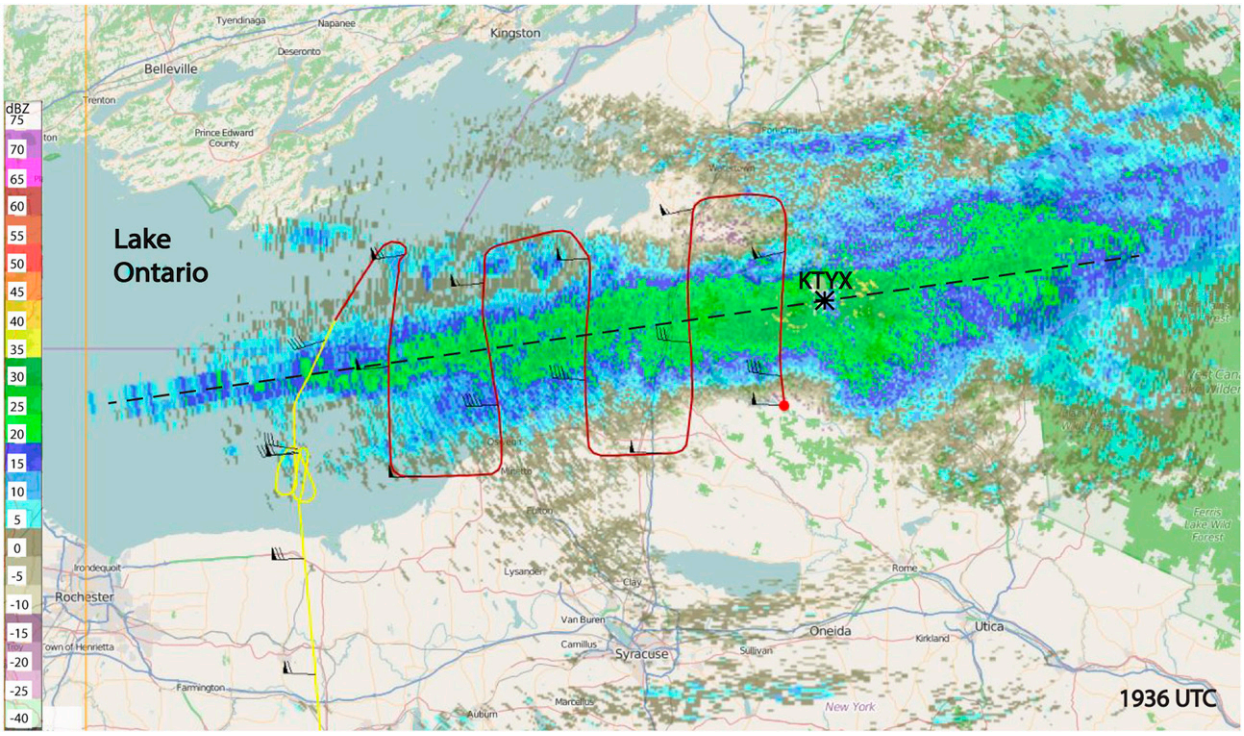

FIG. 6. KTYX 0.5° base reflectivity at 1936 UTC 11 Dec, with UWKA flight track. The black dashed line shows the approximate center of the LLAP band as seen from KTYX.

Convective updrafts and associated turbulence and compensating subsidence are evident at higher levels along the three offshore tracks, up to the top of the LLAP band (Figs. 8a–c). No shallow convective updrafts or BWERs occur along track 5. Vertical velocities appear more benign along this track, with prevailing ascent over the entire width of the transect. Echoes along track 5 also are smoother, whereas a more finescale Z structure is present along the offshore tracks. This indicates a transition from convective updrafts to stratiform lifting and precipitation upon landfall. This second observation supports both hypotheses (section 1).

Third, Z_{WCR} tends to peak aloft, rather than near the surface. This applies along all five tracks (Fig. 7), and applies not only to the margin, but also to the core of the LLAP band. For the sake of consistency and objectivity, we somewhat arbitrarily define the "core" as a 15-km-wide segment of the LLAP band centered on the strongest vertically integrated (surface to 3 km AGL) WCR updraft (red bars in Fig. 7). The LLAP margins are the lateral regions surrounding the core, out to the LLAP band edge or to the end points of the flight leg. We will revisit findings related to this definition later.

Last, we point to a few other observations that may affect snow growth. The rapid small-scale variations between up- and downdrafts in the lowest 0.5–1.0 km, most obvious along track 5 (Fig. 8e) probably are due to boundary layer turbulence (Geerts et al. 2011). Similar high-amplitude, small-scale vertical velocity variations near the LLAP-band cloud top, again most obvious along the inland tracks, may be shear driven as well. And the thin clouds above the LLAP echo tops contain internal gravity waves, likely triggered by penetrating convection within the LLAP band. Such waves are highlighted along track 1 (Fig. 8a) but they are present elsewhere also.

b. *Frequency-by-altitude diagrams*

To explore changes in the LLAP band from offshore (track 1) to inland (track 5) using all 12 legs flown on this day, frequency-by-altitude diagrams (FADs) for WCR Z and WCR w are constructed for each of the five tracks. An example of these FADs is presented for track 3, in Fig. 9. The frequencies shown are normalized by the total count at all levels. The data presence line shown on the right margin in Fig. 9 shows data drops at the three flight levels along track 3 (Table 2) because of the WCR radar blind zone, about 250 m wide for the up and down antennas combined. The reduction in frequencies at these levels is an artifact of the 2D normalization of the counts. For Z (Fig. 9a), profiles of the mean and a series of percentiles are shown. Mean reflectivity is calculated in units of $mm^6 m^{-3}$ and expressed in dBZ, for the WCR and other radars

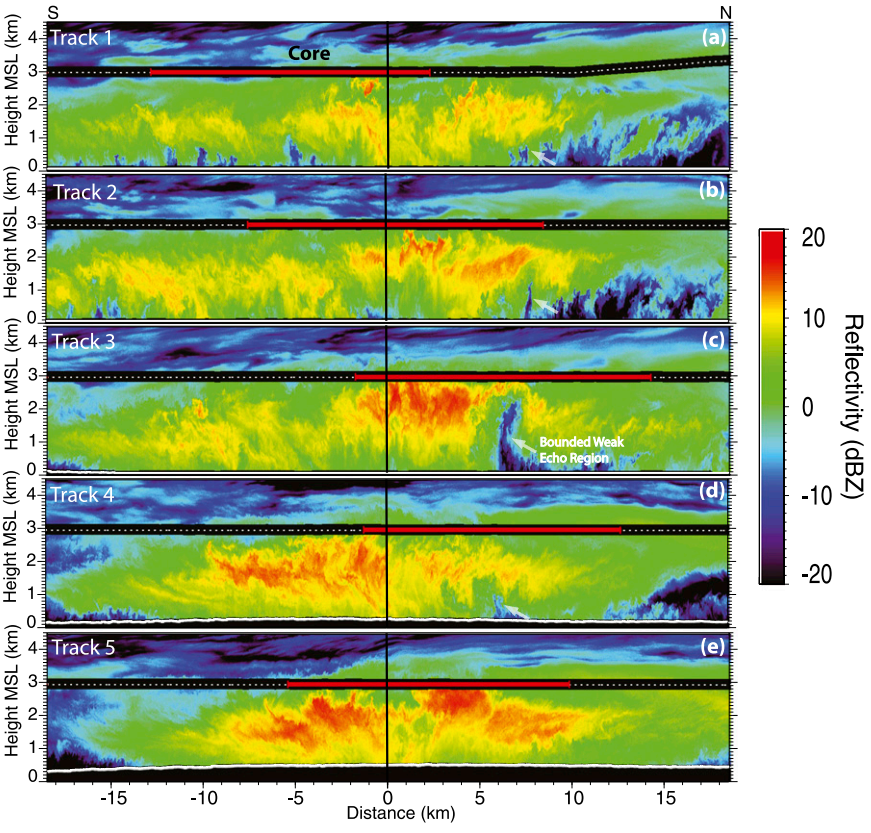

FIG. 7. (a)–(e) WCR transects of reflectivity corresponding to individual flight legs over tracks 1–5 from south to north. The times for the legs are shown in Table 2. The WCR blind zone is in black, and flight level is shown as a dotted white line centered in the blind zone. "Core" sections of the band are denoted by red bars at flight level. The distance x is relative to the band center as seen from KTYX (as in Fig. 6). The white arrows in (a)–(d) indicate the location of strong updrafts, as evident from Fig. 8.

discussed herein. For w (Fig. 9b), profiles of the mean and the mean ± 1 standard deviation (σ_w) are shown. These statistical quantities are used below to assess LLAP band evolution as it makes landfall.

The Z_{WCR} profiles summarized in Fig. 9a agree with the third observation mentioned in section 4a, that Z_{WCR} tends to peak well above the surface, specifically between 1.2 and 1.9 km AGL (Fig. 9a). We first

TABLE 2. Summary of all UWKA flight legs in IOP2b.

Leg No.	Track No.	Leg start (UTC)	Leg end (UTC)	Mean flight level (m, MSL)	Mean temperature (°C)	Mean vertical velocity ($m\,s^{-1}$)
1	1	1841:00	1848:30	2970	−25.1	0.26
2	2	1853:00	1900:45	2956	−25.4	0.50
3	3	1905:05	1912:30	2958	−25.3	0.39
4	4	1916:55	1924:55	2958	−25.9	0.47
5	5	1928:20	1935:58	2955	−25.9	0.24
6	4	1942:30	1951:50	1704	−16.0	0.60
7	3	1959:00	2006:20	1696	−16.1	0.39
8	3	2009:00	2017:00	1696	−16.0	0.60
9	3	2019:39	2029:08	1696	−16.0	0.32
10	4	2033:07	2041:38	1701	−16.0	0.56
11	3	2046:45	2057:00	1192	−12.5	0.29
12	3	2059:50	2104:15	1022	−10.7	0.42

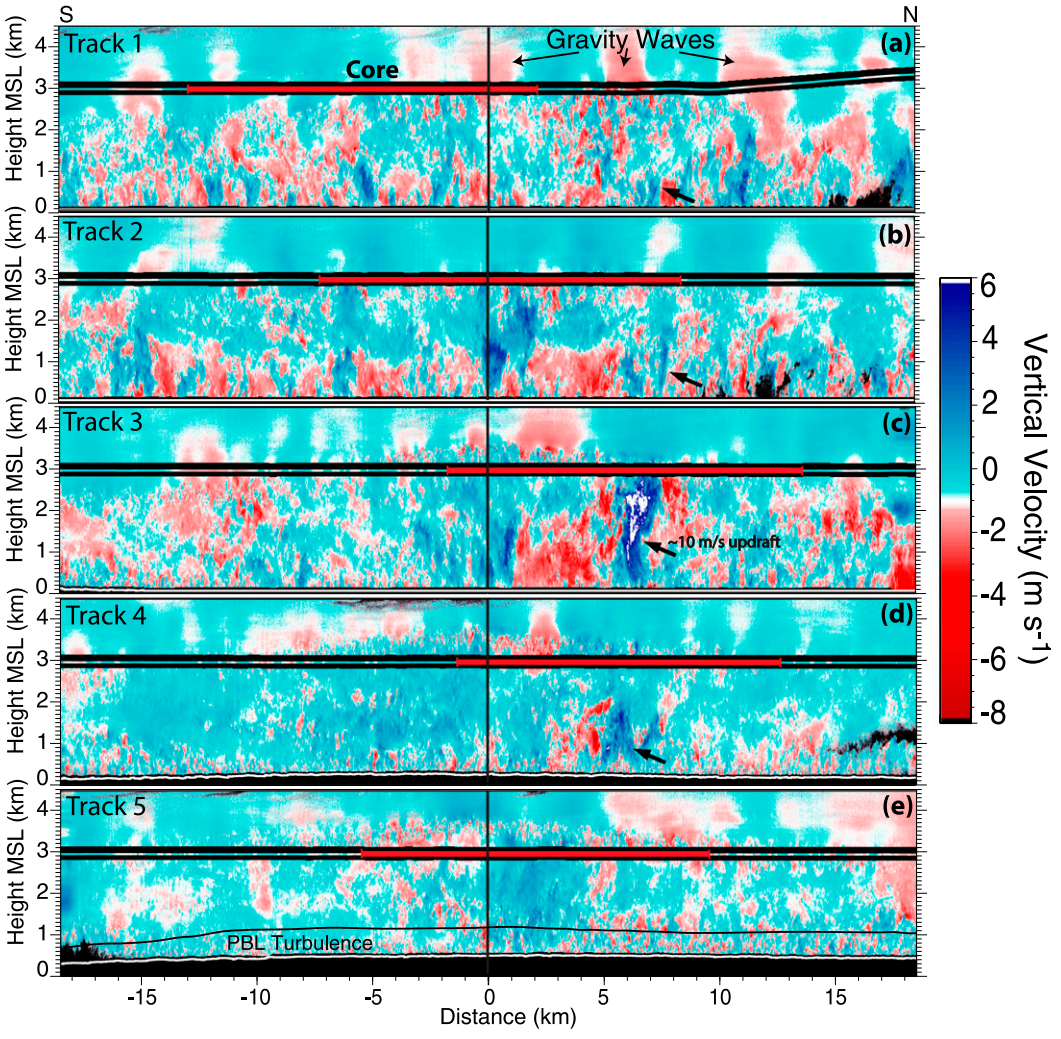

FIG. 8. (a)–(e) As in Fig. 7, but for WCR Doppler hydrometeor vertical velocity. The color scale is centered at $-1\,\mathrm{m\,s^{-1}}$ to account for the typical fall speed of (unrimed) snow, so blue (red) indicates updrafts (downdrafts). Gust probe (air) vertical velocity is shown at flight level, with a color scale of the same range but centered at $0\,\mathrm{m\,s^{-1}}$. The black arrows in (a)–(d) are the same as the white arrows in Fig. 7.

ascertain whether the low-level Z decrease toward the surface is real.

c. *Uncertainties in WCR reflectivity profile*

The 95-GHz radar Z measurements are affected by attenuation due to water vapor and oxygen (<0.5-dB two-way attenuation down to the surface for the humidity profiles shown in Fig. 4), and due to liquid cloud droplets. Thus WCR Z may decrease toward the ground partly due to attenuation, rather than particle scattering. We can improve the Z_{WCR} estimate due to particle scattering alone by removing the estimated two-way path-integrated attenuation due to cloud droplets. This attenuation is about $9.2\,\mathrm{dB\,km^{-1}\,(g\,m^{-3})^{-1}}$ of LW at temperatures between 0° and 20°C (e.g., Vali and Haimov 2001), but less certain for supercooled LW. Recent LW absorption models for the microwave region and subfreezing temperatures (Kneifel et al. 2014; Rosenkranz 2015; Turner et al. 2016) suggest a slightly lower attenuation rate. Here we use the model in Turner et al. (2016), which gives a two-way attenuation rate at 95 GHz ranging between 6.9 and $8.8\,\mathrm{dB\,km^{-1}\,(g\,m^{-3})^{-1}}$ in the relevant temperature range (−28° to −7°C). The profile of LWC is estimated by the MPR at SC, which is located between tracks 3 and 4 (Fig. 2). The average radiometer LWC profile is shown in Fig. 10 together with flight-level LWC measurements for all flight legs during this event. There is much uncertainty about the retrieval of LWC from a microwave radiometer, because there is no clear

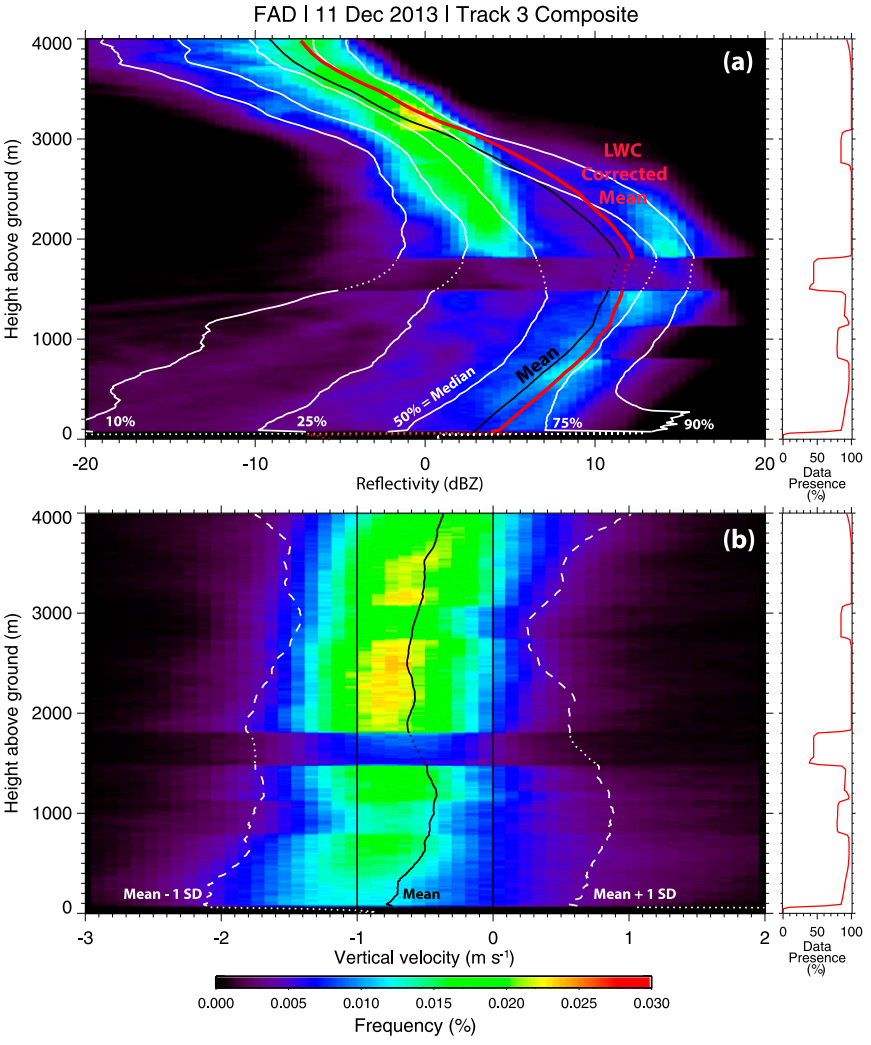

FIG. 9. WCR FAD of (a) reflectivity and (b) hydrometeor vertical velocity for all six passes over track 3. In (a), the black line is the profile of the mean Z, and the adjacent white lines are the 10th, 25th, 50th, 75th, and 90th percentiles. The red line is the mean Z profile "corrected" for attenuation by cloud droplets using the LWC profile in Fig. 10. The "data presence" profile (the fraction of pixels with Z data at each level) is shown as a red line on the right of (a) and (b). In (b), the black line is the mean profile and the dashed white lines are the mean ± 1 standard deviation (SD).

absorption feature due to droplets, and little information about vertical distribution (e.g., Crewell et al. 2009). Indeed in situ measurements do not correspond well with the radiometer profile. Yet the liquid water path (LWP) estimated from three flight levels along track 3 (the only track with three levels of data) is fairly close to the radiometer LWP. Both estimations of LWP yield a path-integrated attenuation of at most 2 dB near the surface. We remove range-dependent Z loss by LWC attenuation (assuming the MPR LWC profile, for lack of better data) from all WCR Z values, for all flight legs. The resulting mean Z profile, accounting for this attenuation, is shown as a red line in Fig. 9a for track 3. Hereafter, the LWC-"corrected" Z profiles will be used without further mention, since the correction (albeit uncertain) is rather small.

In addition to attenuation by gases and droplets, millimeter-wavelength radar Z may be affected by power extinction by ice particles, mainly nonspherical particles larger than 1 mm (e.g., Li et al. 2001; Matrosov and Heymsfield 2008). For instance, horizontal radar measurements yield extinction values of $0.9\,\mathrm{dB\,km^{-1}\,(g\,m^{-3})^{-1}}$ in dry snow (Nemarich et al. 1988). Such particles obviously are not very realistic, and the effects of this range-dependent loss are not easily accounted for. To quantify this loss, we compare WCR mean

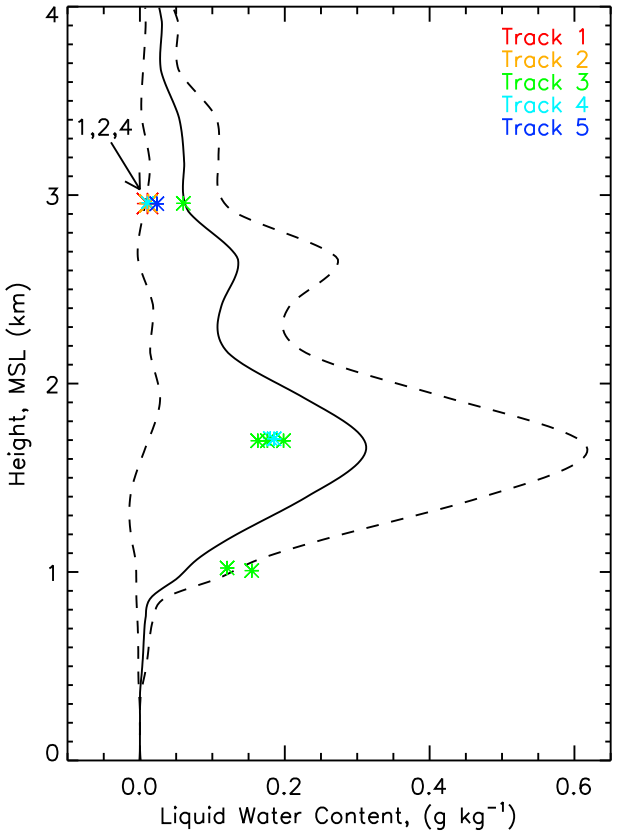

FIG. 10. LWC profile estimated from a passive microwave radiometer at SC (Fig. 2) The average (mean ±1 standard deviation) over the 1905–2105 UTC period is shown as a solid (dashed) line. Also shown is the average flight-level LWC from the core sections of UWKA flight legs, color coded by track location.

Z profiles from legs flown at various altitudes over the same track (track 3) (Fig. 11a). The expectation is that Z profiles at greater range (e.g., a low-level echo observed from a high flight level) suffer more from the attenuation by ice particles than those at close range to the radar (e.g., a low-level echo from a lower flight level). The decrease in Z toward the surface is similar for all three flight levels (3.0, 1.7, and 1.0 km MSL), starting between 1.3 and 1.9 km MSL and amounts to 5–9 dB, from that level down to the surface. The Z profile collected at the lowest flight level (1.0 km MSL) shows an upward increase in Z toward the peak some 500 m above flight level, and a decrease in Z between that level and the surface, comparable to the Z profiles from the other flight levels. This indicates that power loss due to extinction by ice particles is rather small as well, at least on average along flight legs.

Li et al. (2005) show that the surface backscattering from an open water surface (the water surface radar cross section σ_o) can be used for the calibration of airborne or spaceborne W-band radars, due to the relative insensitivity of σ_o to surface winds and water roughness at small incidence angles (<10° from zenith). Lake Ontario was still ice free on 11 December 2013, and the surface winds below the UWKA flight track are within the range of those examined by Li et al. (2005). Therefore the reduction in σ_o over Lake Ontario is a measure of two-way path-integrated attenuation of the WCR beam, by gases, droplets, and ice crystals.

We plot the WCR σ_o for the same three flight legs over track 3 in Figs. 11b–d, starting at the shoreline on the southern end (Fig. 2) to exclude the portion over land. Also shown in Figs. 11b–d is the time–space matched Z_{DOW} near the level of maximum Z (1.6 km MSL). The X-band attenuation of Z by gases, droplets, and ice particles (except very large ones) is insignificant. The highest σ_o values on the margins of the LLAP band transect in Figs. 11b–d represent those of nearly clear-air values (little liquid water and small ice crystals only). Inside strong echoes (DOW Z > ~20 dB) WCR σ_o is reduced as seen from a high flight level (3.0 km, Fig. 11b), but not as seen from a low flight level (1.0 km, Fig. 11d). The σ_o reduction is as large as 13 dB (cf. the peak value) at x = 21 km at the 3.0-km flight level (Fig. 11b). This point corresponds with the BWER highlighted in Fig. 7c. WCR and DOW data indicate elevated Z values over ~7 km to the south of this BWER (Figs. 7c and 11b), and a sustained σ_o reduction about half as large as the peak (~6 dB). The large WCR σ_o reduction in the BWER probably is dominated by a high LWP below flight level, and the smaller σ_o reduction immediately to the south is probably largely due to extinction by ice particles. The peak σ_o reduction at the 1.7-km flight level (9 dB, x = 9 km in Fig. 11c) also corresponds with a BWER. At the lowest flight level (1.0 km, Fig. 11d), any σ_o reduction is very small, but still largest in areas with heavy snowfall (high DOW Z).

In summary, the Z_{WCR} profiles locally are attenuated by high concentrations of droplets and large ice crystals, especially in or near the BWERs. The correction for a mean LWC profile is only approximate and does not account for the extinction by ice particles. But the mean Z_{WCR} profiles are rather insensitive to flight level (Fig. 11a) and the σ_o reduction generally amounts to only a few dB (Figs. 11b–d), less than the observed ~7-dB decrease (from peak to surface) in the mean Z profile for all legs along track 3. Thus, this decrease is real, although it may be exaggerated.

d. Evolution of WCR reflectivity and vertical velocity profiles from lake to land

The mean Z_{WCR} profile (corrected for attenuation by liquid water) peaks well above ground level along track 3 (Fig. 9a). This suggests that most of the snow growth

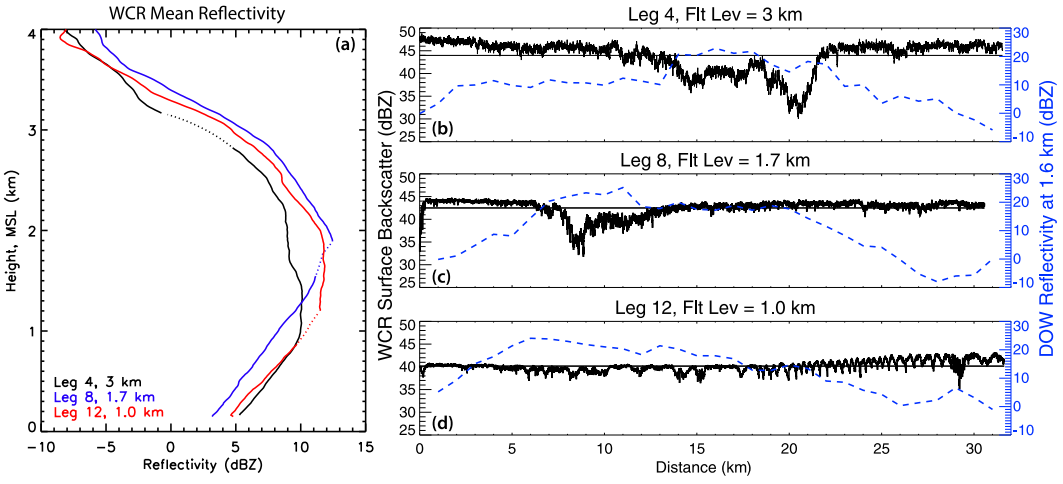

FIG. 11. (a) Profiles of mean WCR Z from three legs (4, 8, and 12, see Table 2) flown along track 3 at different altitudes (3.0, 1.7, and 1.0 km MSL). (b)–(d) WCR surface radar cross section σ_o (bold black line) and 1.6 km MSL (1.5 km AGL) DOW Z (dashed blue line) for the same legs along track 3, starting (at $x = 0$) at the southern shoreline of Lake Ontario. The thin black line is the mean σ_o along each leg.

occurs aloft, and that snow mass and snowfall rate peak well above the ground (Pokharel and Vali 2011). The peak in Z_{WCR} is elevated along the other tracks also (Fig. 12a). The height of the peak Z increases from west to east. A significant increase in height of this maximum occurs between tracks 2 and 3, and remains high (~1.8 km MSL) over track 4, before a large decrease in altitude is seen over track 5 (~1.5 km MSL). High-reflectivity values in the dendritic snow growth zone [about −12° to 18°C, corresponding to 1.2–2.1 km MSL (Fig. 4)] are not uncommon in lake-effect storms (e.g., Waldstreicher 2002) or nimbostratus in general (e.g., White et al. 2003). But the decrease of Z_{WCR} below this zone may indicate hydrometeor lofting, in support of hypothesis 1. The echo top of rather strong echoes, 5 dBZ for WCR (this value corresponds with a significant decrease in Z with height in both core and margin areas, Fig. 7), increases from track 1 to track 3, and remains elevated inland (Fig. 12a). This indicates that while Z values are elevated aloft through hydrometeor lofting by deep updrafts mainly along track 3, these high values are maintained over land.

The near-surface mean Z_{WCR} is lowest on track 1 and highest on track 5 (Fig. 12a), consistent with the observed increase in NCEP stage-IV precipitation over that distance (Fig. 1). The average Z_{WCR} in the lowest 500 m is 4 dB higher along track 5, over the Tug.

Changes in Z are related to changes in w: the mean hydrometeor vertical velocity $\overline{w}$ is substantially larger along track 5 than along the other tracks at most altitudes (Fig. 13a), lending support to the stratiform ascent hypothesis; $\overline{w}$ is rather high along track 3 as well, at low levels, due to the very strong updraft highlighted in Fig. 8c. It is possible that the higher $\overline{w}$ value along track 5 is at least partly due to a larger hydrometeor fall speed over the other tracks, due to riming in the convective updrafts offshore. Rimed particles have a higher fall speed (Locatelli and Hobbs 1974). It is impossible to partition WCR w into air vertical motion and particle fall speed. Fall speed can be estimated at flight level as the difference between gust probe (air) vertical velocity and nearby WCR w (average close-range values from up and down antennas), but that estimate has an uncertainty of ~1 m s^{-1}. This approach yields fall speed estimates of 0.7–1.5 ± 1 m s^{-1} for all 12 flight legs, the highest value being along track 3 at a flight level of 1.7 km. The mean fall speed estimate for the offshore legs is lower than for the onshore legs. While these estimates are low compared to the fall speed of graupel, they do not exclude the possibility of rimed particles in some areas.

Convective vertical motions have a higher second moment (standard deviation, σ_w) than does stratiform ascent, and they tend to display a positive third moment (skewness, μ_w, a normalized unit), as updrafts are stronger and more local than compensating downdrafts (e.g., Moyer and Young 1991; Hogan et al. 2009). This positive skewness is evident in Fig. 9b for track 3, where the mean (black line) is seen to remain higher than the peak frequency values (mode) at most levels, especially near 2 km MSL. Some vertical velocity values exceed the upper limit shown (>2 m s^{-1}), particularly at low levels. The large σ_w value along track 3 (>1.0 m s^{-1} at most levels, Figs. 9b and 13b) is the result of a combination of linear convection (LLAP band secondary circulation) and the mostly shallow convective cells

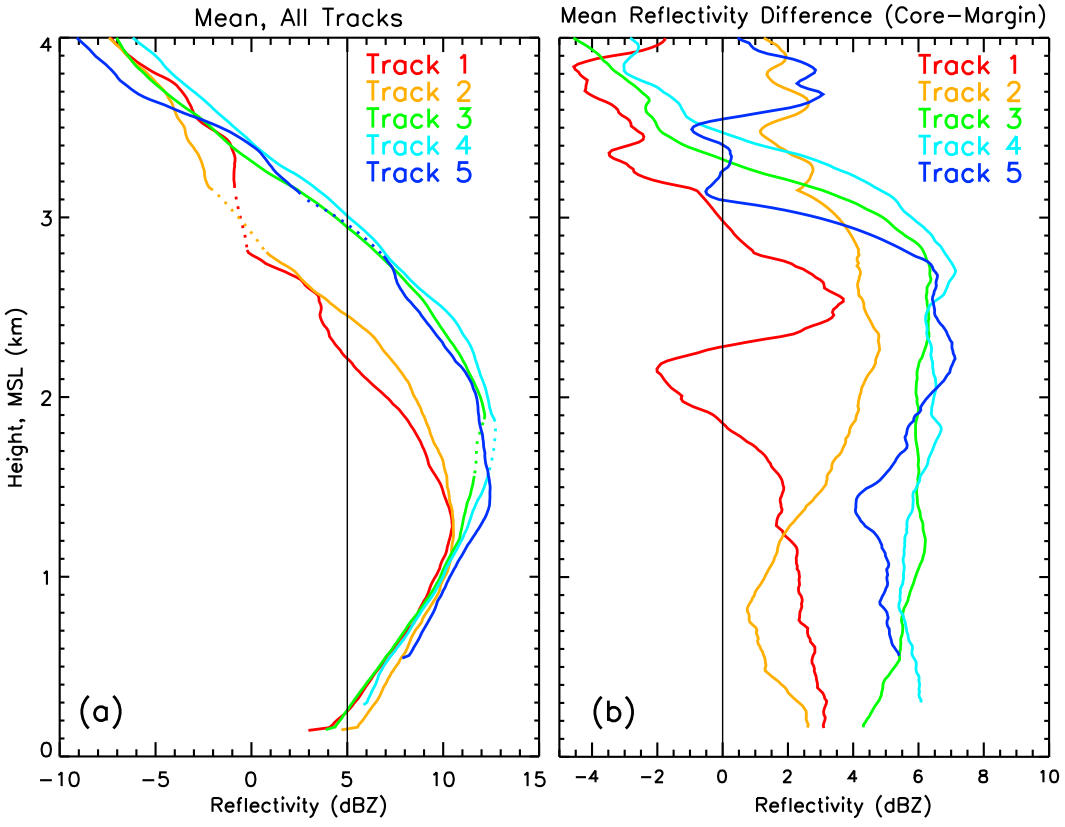

FIG. 12. (a) Mean WCR reflectivity profiles for all flight legs over each track and (b) the core-margin mean reflectivity difference.

seen offshore (Fig. 8). The values of σ_w and μ_w are higher for the offshore tracks (1–3) than onshore tracks, especially at low levels (Figs. 13b and 13c). Track 5 has the lowest values of σ_w and μ_w, particularly below ~1.5 km MSL, indicating that precipitation is mostly stratiform there. The secondary circulation is still present, but it has broadened and weakened (Fig. 8e). This result supports the expectations of both hypotheses proposed in section 1.

Some differences between the five tracks (discussed above) may be related to the exact location of the flight legs relative to the band's center. For this reason all legs are analyzed over the longest common distance (~37 km). The WCR-defined 15-km-wide cores (section 4a) correspond reasonably well with the belt of highest Z_{KTYX} (Fig. 7). The Z_{WCR} contrast between core and margin is strongest where the LLAP band is best developed, along tracks 3–5 (Fig. 12b). The 5-dBZ echo top is higher in the LLAP band core than the margin, and this echo-top bulging also is more defined along tracks 3–5 (Table 3). There is a positive vertical velocity difference between core and margin along all tracks (Fig. 13d) at most levels. This difference (~0.5 m s^{-1} at midlevels) quantifies the strength of the secondary circulation over the width of the LLAP band. (It may be stronger yet because the particle fall speed may be higher in the core.) This positive vertical velocity difference is consistent with the observed Z streaks slanting in the margin, away from the core (Fig. 7), and with the observed low-level confluence and upper-level diffluence (Bergmaier et al. 2015). There is no evidence for circulation strengthening toward the east. Along track 5 the vertical velocity difference is smaller, in fact the low-level vertical velocity is nearly the same in the core and the margin, indicating that widespread ascent over the Tug Hill dominates over the secondary cross-LLAP circulation.

5. Particle size distributions and riming amount

a. *In situ particle size measurements*

The stratiform ascent hypothesis expects an increase in particle size toward the ground, as snow grows in supercooled cloud layers. Particle size distributions are measured at flight level (CIP, 2D-P) and on the ground at SC (the MIPS PARSIVEL disdrometer). The PARSIVEL data averaged over the 2-h period (Fig. 14) show that small particles are most common with mean

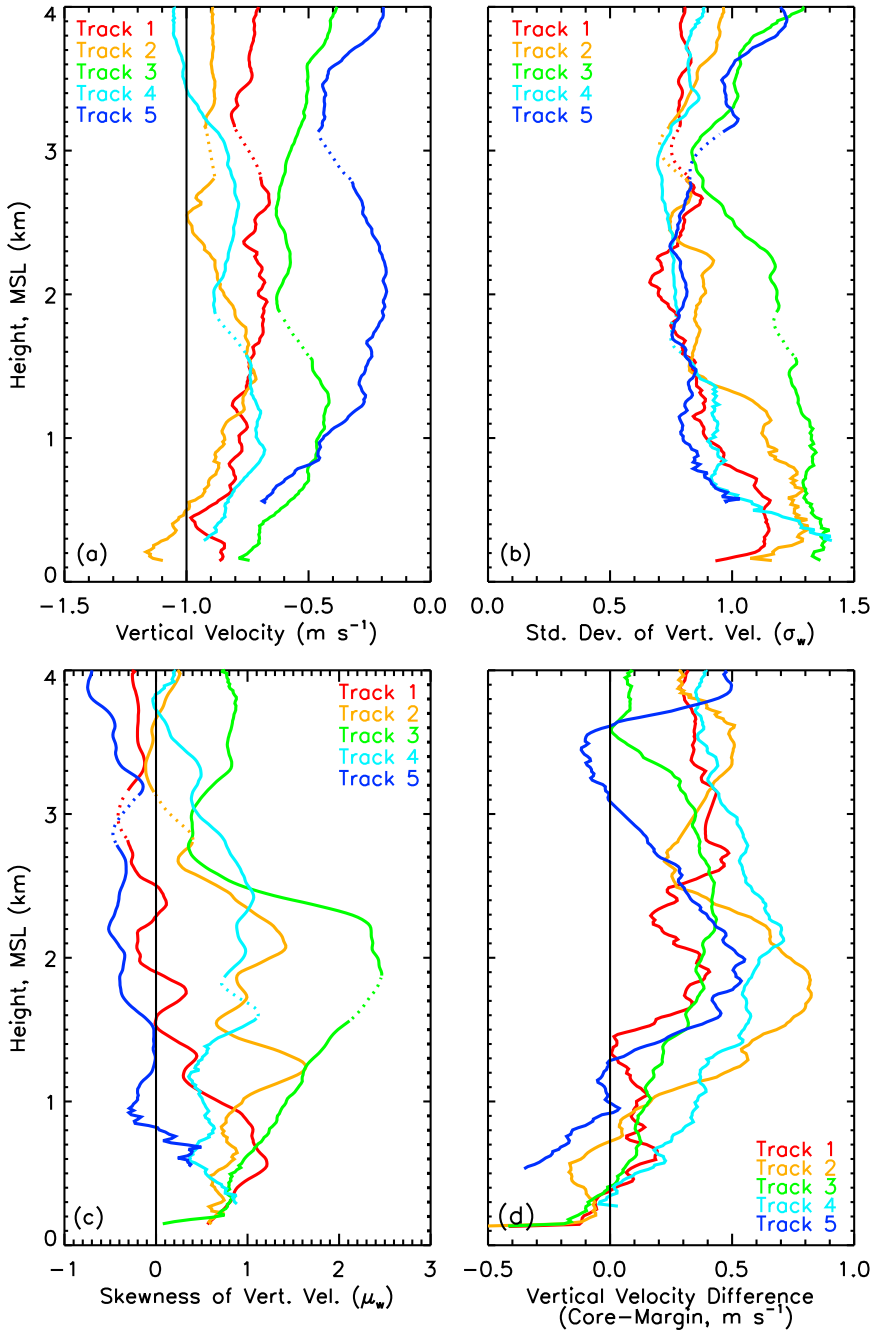

FIG. 13. Profiles of the moments of the composite WCR hydrometeor vertical velocity (w) distribution for IOP2b, stratified by flight track (color coded). (a) Mean $\overline{w}$, (b) standard deviation σ_w, (c) skewness μ_w, and (d) difference between core and margin ($\overline{w}_{\text{core}} - \overline{w}_{\text{margin}}$).

concentration peaking around 0.5 mm. But a significant fraction of particles is larger than 0.8 mm, and there are some aggregates larger than 3.2 mm. Disdrometer data at SC suggest that this is the case throughout the 27-h-long IOP2 (Minder et al. 2015). Note that the PARSIVEL was developed for rain and has some issues for snow particles (Battaglia et al. 2010).

Flight-level particle size distributions are available for all flight legs, but most legs are in the upper portion of the LLAP band (Table 2). To examine the along-band evolution, CIP and 2D-P size distributions for tracks 1–5 are examined, all at a flight level of 3.0 km MSL (Figs. 15a–d). Ice particle concentrations steadily increase from west to east. The concentration of ice particles is larger in the

TABLE 3. Echo-top height (in km MSL) data from each WCR track and DOW box in the core and margin areas. The echo top is defined as the 5-dBZ level for the WCR and the 9-dBZ level for the DOW (i.e., it refers to rather strong echoes). These thresholds are chosen based on the observed rapid decrease of reflectivity with height (Figs. 11 and 18).

	WCR		DOW	
Track/box	Core	Margin	Core	Margin
1	2.6	2.3	3.4	2.9
2	2.7	2.3	3.2	1.3
3	3.1	2.6	3.2	3.1
4	3.2	2.6	—	—
5	3.1	2.5	—	—

LLAP band core than the margin (Table 4). This is especially true for large particles (>1 mm), where the core: margin ratio in concentration exceeds an order of magnitude on most tracks. Hydrometeors larger than 2 mm are absent on tracks 1–2, but exist at concentrations of 0.5 L^{-1} in the upper band core along track 5 (not shown). High concentrations of large particles are found along track 3 as well, probably due to the strong updraft encountered there (Fig. 8). All this suggests that ice particles are ejected from the core into the marginal anvil by the main LLAP-band updraft and circulation (a "fountain" of ice particles), and that some sorting takes place as large particles remain concentrated near the band core.

Lower-level in situ particle size data are available only for tracks 3–4. The 1.7-km flight level corresponds to a temperature of −16°C (Table 2), that is, near the dendritic growth zone, and the temperature belt of ready growth by vapor diffusion due to the large saturation vapor pressure difference between water and ice. Particles increase in both mean diameter and concentration at lower levels over tracks 3 and 4 (Table 4). The concentration of particles >1 mm is one to two orders of magnitude larger at 1.7 km than at 3.0 km MSL, both in the core and the margin (Figs. 15e,f). The concentration of particles larger than 3.2 mm is ~20 times larger at 1.7 km than at 3 km MSL, and is ~3 times larger at 1.0 km than at 1.7 km MSL, according to 2DP data in the core on track 3 (Fig. 15g). There are at least 10 times fewer hydrometeors around 5 mm in size to compared to those ~0.5 mm, even at the lowest flight level on track 3 (Fig. 15g), but that ratio is only ~3 on the ground, according to the PARSIVEL disdrometer data (Fig. 14). This tremendous increase in concentration of aggregates toward the ground is consistent with DWR measurements, as will be shown in section 6.

b. *Frequency of occurrence of rimed particles*

Fall speed estimates suggest little riming in the LLAP band along its length, at least over the full width of the band (section 4d). The 2D-P and CIP 2D particle images do indicate pockets of rimed particles at flight level (Fig. 16). The examples in Figs. 16a and 16b are collected above the BWER on track 3 (Fig. 7c). Some particles appear more compact (probably rimed), others more open structured (probably less rimed aggregates). Larger rimed particles are encountered at lower flight levels on track 3 (Figs. 16c–f), all in the vicinity of BWERs. Hydrometeors were photographed also on the ground at SC and at NR, using both hand-held cameras and a Hydrometeor Video Sonde (HYVIS) camera. Some photographed particles are rather spherical and appear heavily rimed, with droplets accreted along their edges (Figs. 16g–l). But most particles observed on the ground were less rimed aggregates. Data from the PARSIVEL disdrometer at SC (section 3c) indicate that a small fraction (~10%) of hydrometeors have a fall speed characteristic of graupel during the UWKA flight (not shown), although disdrometer fall speed estimates are uncertain, especially in windy conditions (e.g., Battaglia et al. 2010). In short, riming is not the primary snow growth mechanism in this LLAP band, although local pockets of graupel were present.

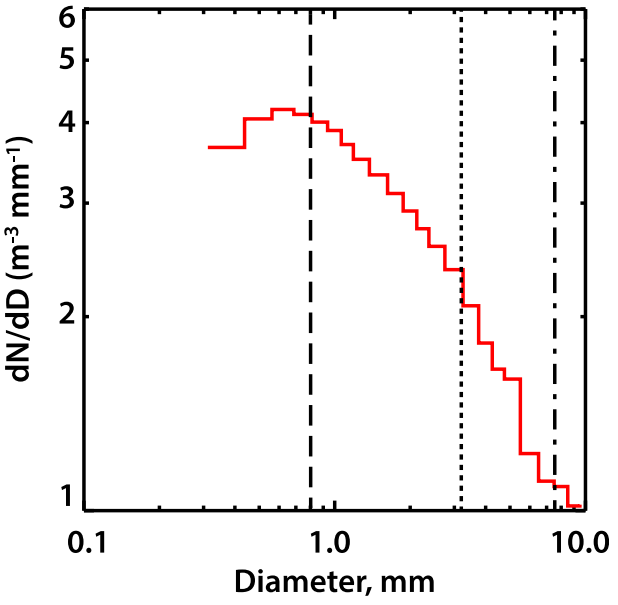

FIG. 14. Mean particle size distribution measured by a PARSIVEL disdrometer at SC between 1905 and 2105 UTC. Vertical lines correspond to W-band (dashed), K-band (dotted), and X-band (dot–dash) size thresholds for Rayleigh–Mie transition.

6. Comparison of multifrequency radar reflectivity profiles

The simultaneous operation of various profiling radars in relatively close proximity allows Z comparisons to be made. As mentioned in section 2f, the comparisons of Z

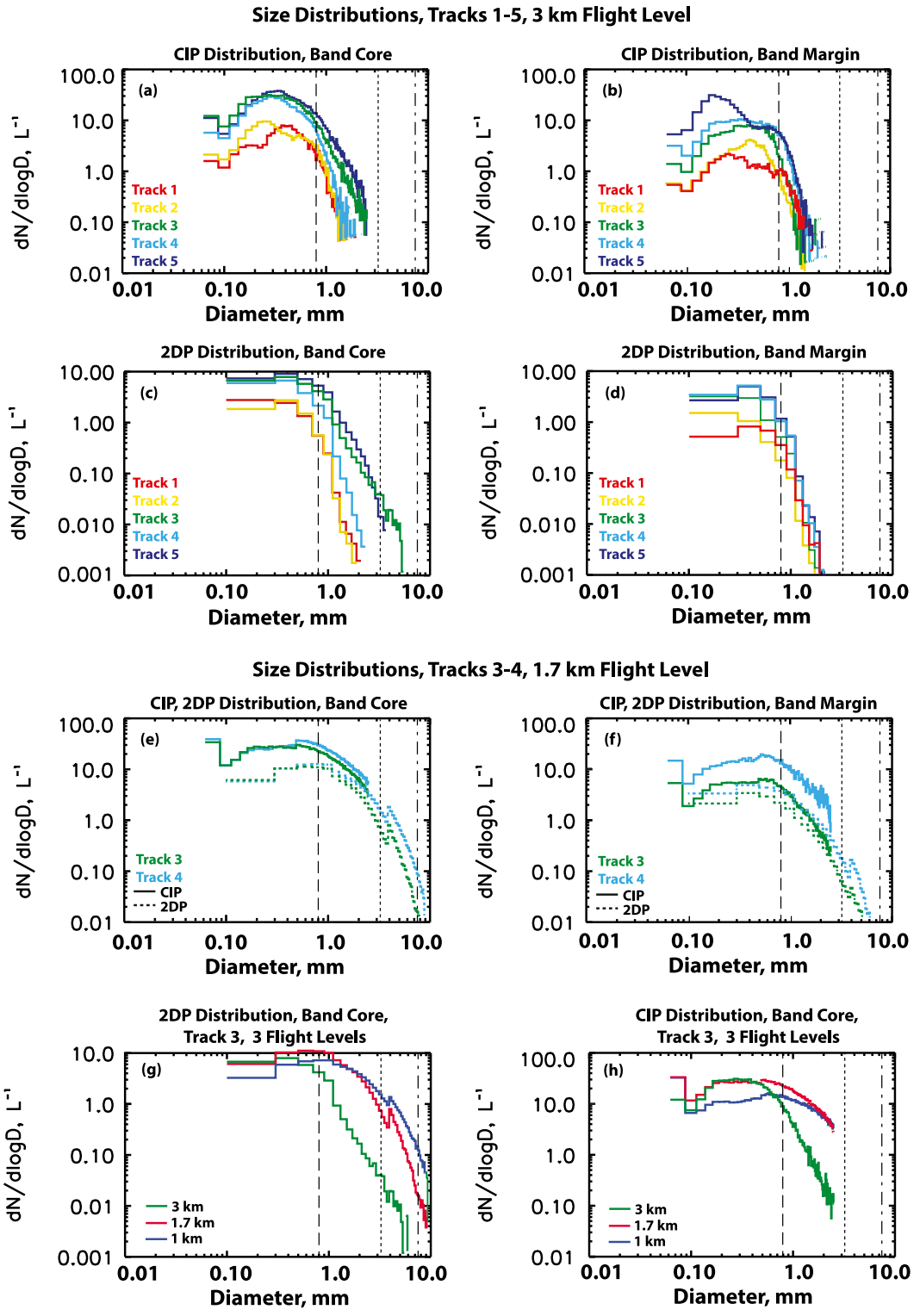

FIG. 15. Mean particle size distributions measured by the CIP and 2D-P probes in the LLAP band (left) core and (right) margin areas, (a)–(d) for tracks 1–5 at 3 km MSL, and (e),(f) for tracks 3 and 4 at 1.7 km MSL. (g) 2D-P and (h) CIP size distributions at three flight levels (3.0, 1.7, and 1.0 km) for the core over track 3. Approximate size thresholds for Rayleigh–Mie scattering transition for W band (dashed line), K band (dotted line), and X band (dot–dash line) are denoted by vertical lines.

TABLE 4. Flight-level particle concentrations and size, averaged for each flight track. The distinction between core and margin is shown in Fig. 7.

Particle concentration					
Flight level (km MSL)	Track No.	2DP (L^{-1}) Core	2DP (L^{-1}) Margin	CIP (L^{-1}) Core	CIP (L^{-1}) Margin
3.0	1	2.1	0.7	8.9	3.5
	2	1.8	1.2	11.3	4.8
	3	6.7	2	63.2	1.2
	4	5.3	3.1	33.2	1.8
	5	7.8	3.1	61.9	2.9
1.7	3	10.7	3.9	175.9	38.2
	4	11.9	4.3	364.6	89.4
Mean particle diameter					
Flight level (km MSL)	Track No.	2DP (mm) Core	2DP (mm) Margin	CIP (mm) Core	CIP (mm) Margin
3.0	1	0.31	0.39	0.32	0.32
	2	0.35	0.29	0.28	0.33
	3	0.41	0.30	0.28	0.31
	4	0.35	0.35	0.28	0.31
	5	0.43	0.37	0.33	0.22
1.7	3	0.72	0.53	0.42	0.38
	4	0.86	0.58	0.47	0.43

values from radars at different frequencies are qualitative since most radars are not rigorously calibrated, the radar resolution volumes are not coincident in time or space, and the different radar illumination volumes do not match (profiling vs low-elevation scanning). Therefore, we examine profiles of DWR but do not apply any dual-frequency algorithms for the assessment of actual particle size or precipitation rate.

a. DOW

The interpolated Z_{DOW} data (section 2d) are collected within 10-km-wide boxes centered over the five UWKA flight tracks (Fig. 17). From its site at Southwick Beach, the DOW has excellent low-level coverage over Lake Ontario, but not over inland tracks 4 and 5. The lowest beam unblocked by terrain is rather high above ground level over the inland boxes (tracks 4 and 5, Fig. 17), and low-level Z in most inland directions appears attenuated there, presumably by trees or other obstacles. Therefore, Z_{DOW} profiles are examined only in the offshore boxes 1–3.

The mean Z_{DOW} profiles in these three boxes (Fig. 18a) show a slight intensification from box 1 to 3 (toward the shore), consistent with WCR observations, but only a benign decrease in Z from midlevels (~1.5 km MSL) toward the surface; which is inconsistent with WCR observations (Fig. 12a). This departure between DOW and WCR observations produces an increase in $DWR_{X,W}$ from 1 to 2 km MSL to near the surface, where it exceeds 10 dBZ (Fig. 18a). This indicates growth in particle size, which is likely due to aggregation at these low levels.

A suitable Z_{DOW} value defining the top of the LLAP band, chosen similarly to WCR echo-top threshold, is 9 dBZ. This echo-top height is higher in the core than in the margin (defined by WCR data) (Table 3). Hydrometeor lofting (mainly in BWERs) and particle sorting in the divergent flow aloft may explain the high $DWR_{X,W}$ values around 3 km MSL (Fig. 18a), mainly in the core, even though the mean particle sizes are rather small at that level (section 4a).

b. KTYX

Profiles of level-II KTYX (location shown in Fig. 2) reflectivity, averaged in the same five boxes, are shown in Fig. 18b. No data are available below ~0.5 km MSL because KTYX is located on the Tug (Fig. 17; Brown et al. 2007). Below 1.8 km MSL, mean Z_{KTYX} increases from west to east, consistent with WCR and DOW data. This increase explains the zonal gradient in NCEP stage-IV precipitation across the Lake Ontario shoreline (Fig. 3). Offshore, this increase is comparable to that of the DOW (Fig. 18a), although the DOW captures the low-level LLAP intensification toward the shoreline much better due to its location. The inland increase of Z_{KTYX} at low levels provides strong evidence of the snowfall enhancement from this LLAP band as it made landfall. The Z_{KTYX} profiles suggest snow growth down to the lowest levels, particularly onshore (tracks 4 and 5), in contrast with the WCR profiles, and even in mild disagreement with the DOW profiles (offshore only). The S-band Z_{KTYX} is due to Rayleigh scattering even for the largest hydrometeors. Some low-level snow aggregates may behave as Mie scatterers at X band, as suggested by the PARSIVEL measurements (Fig. 14). The low-level increase in $DWR_{S,W}$ (Fig. 18b) again provides evidence of low-level snow growth, likely by aggregation, in all regions where KTYX observations and thus $DWR_{S,W}$ profiles reach low levels; especially onshore (Fig. 18b). The high values of Z_{KTYX} and $DWR_{S,W}$ aloft in the distant offshore boxes are at least partly due to beam smearing where Z rapidly decreases with height.

KTYX dual-polarization variables were explored as well (not shown). The differential reflectivity Z_{DR} is remarkably small at all levels and in all boxes, averaging between −0.6 and 0.0. The differential phase (K_{DP}) values are around 0.0. Both Z_{DR} and K_{DP} increase slightly with height. The correlation coefficient (ρ_{hv}) values are high, averaging between 0.97 and 1.0. There is rather little variation in dual-polarization variables in the LLAP band, although there are some

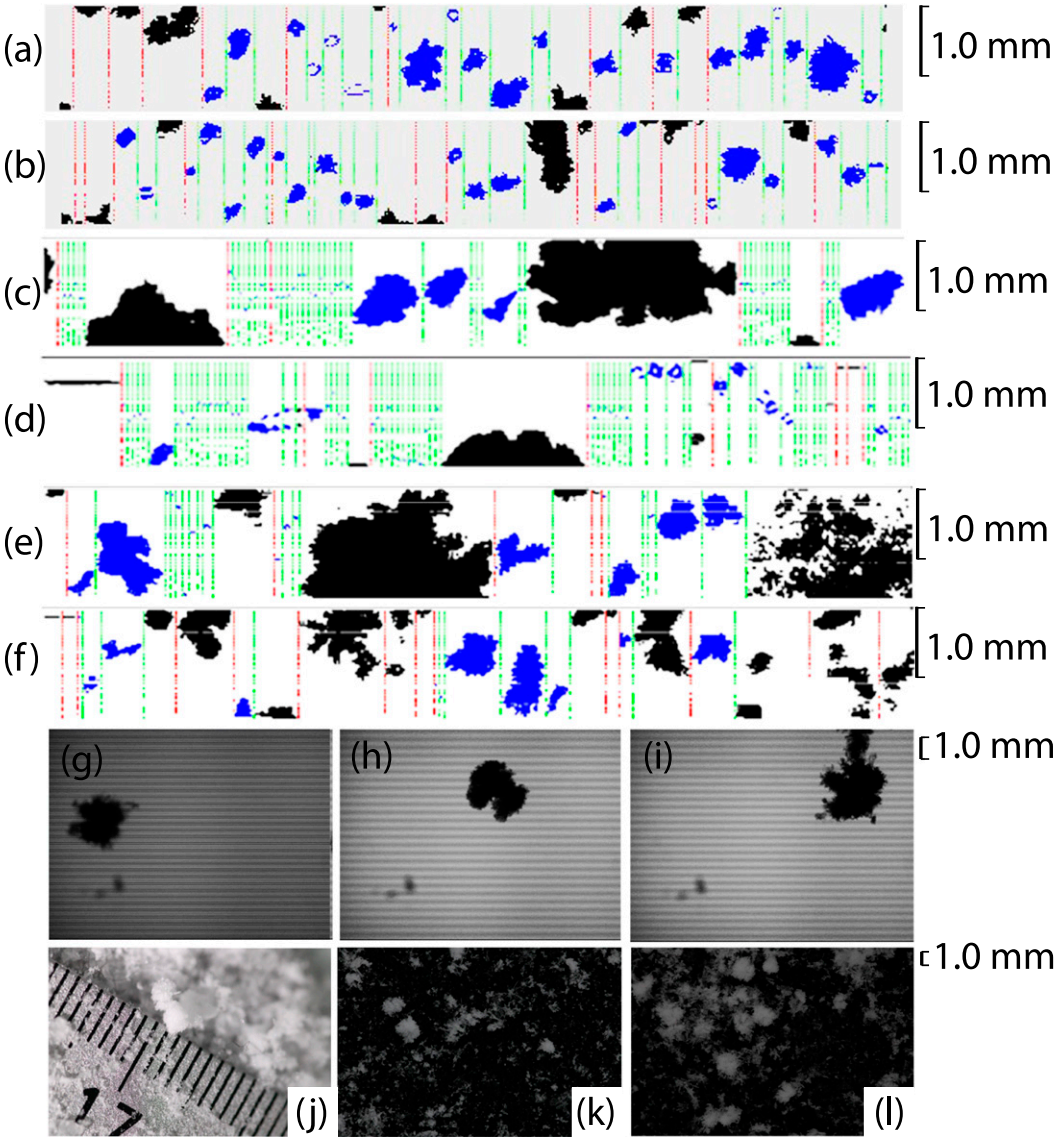

FIG. 16. CIP images of particles at a flight level of (a),(b) 3 km MSL at 1907 UTC; (c),(d) 1.7 km MSL at 2004 UTC; and (e),(f) 1.0 km MSL at 2054 UTC, all on track 3. Particle images from a HYVIS camera at the NR site at (g) 1914, (h) 2032, and (i) 2042 UTC. Hand-held camera images (j) at SC at 2027 UTC and at NR at (k) 2028 and (l) 2041 UTC. For each row, the scale is shown on the right.

cells with enhanced Z, higher Z_{DR} and lower ρ_{hv} offshore, which indicates that they may contain graupel. In general, the low Z_{DR} values, the high ρ_{hv} values, and the rapid decrease of Z_{KTYX} from ~3 km down to the ground level (Fig. 18b) indicate little riming, a dominance of small ice crystals aloft, and dry snow aggregates at low levels (e.g., Kumjian 2013).

c. *Radar comparison at the MRR array*

WCR data collected within 15 km of each of the four MRR sites is compared to the MRR, XPR, and KTYX data, averaged over the same period (1905–2105 UTC). The SB site is primarily compared with track 3 data, the SC site with track 4, the NR site with tracks 4 and 5, and the UP site with track 5 (Fig. 2). The color code for these track sections and the Z profiles at these four sites (Fig. 19) is an extension of the one used to distinguish the five UWKA tracks. The four sites line up well with the axis of the LLAP band during the period of interest, with the exception of NR and UP, which were slightly to the south and north of the band's central axis, respectively (Figs. 2 and 6).

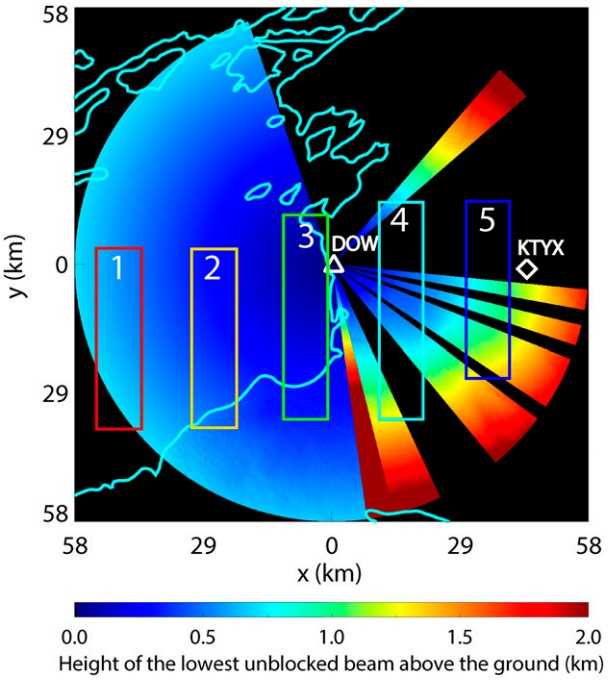

FIG. 17. Map of the height of lowest unblocked DOW beam above the local terrain. The blue line is the shoreline. The five boxes contain the five flight tracks shown in Fig. 2 and are 10 km wide.

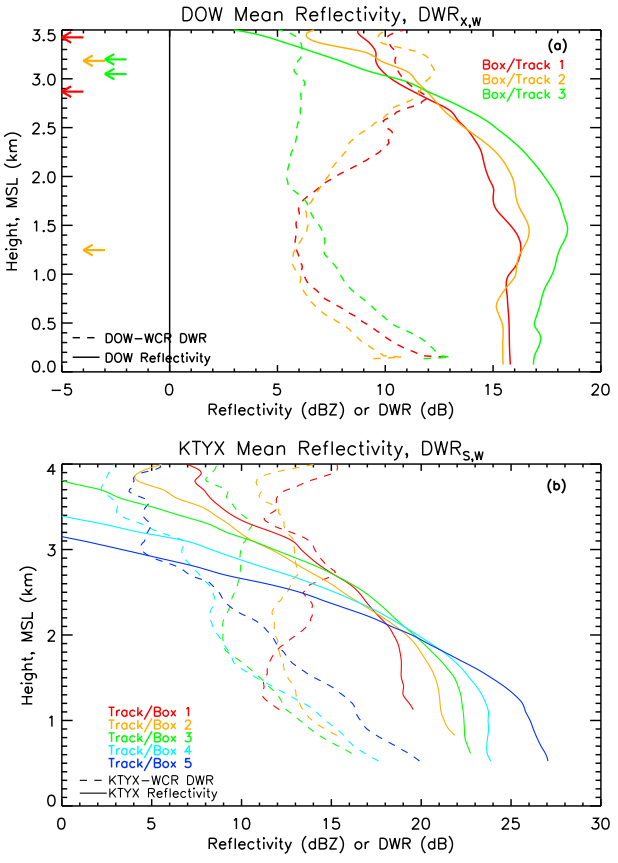

FIG. 18. (a) Profiles of DOW reflectivity (solid lines) and DOW-WCR DWR (dashed lines), color coded by track (or box) locations. Also shown are the DOW echo-top height (level arrows on the left, the upper arrow for the core and lower arrow for the margin). (b) Profiles of mean KTYX reflectivity (solid lines), and KTYX-WCR DWR (dashed lines). All values are averaged within the boxes shown in Fig. 17 between 1905 and 2105 UTC.

Unfortunately no MRR data are available below ~800m AGL as the first two range gates of the Z_{MRR} profiles are removed in processing (Minder et al. 2015). Therefore, the MRRs do not yield insight into low-level snow growth suggested by the $DWR_{S,W}$ and $DWR_{X,W}$ profiles in Fig. 18. The Z_{MRR} at the lowest available levels (say between 0.8 and 1.8 km AGL) is highest near the shore (SB) and lowest on the Tug (UP) (Fig. 19a). This decrease of mean low-level Z_{MRR} from SB to UP does not agree with the WCR or with KTYX (Fig. 19). The four MRRs were collocated for calibration during OWLeS, in a deep storm, and this yielded average differences no larger than 3 dB. The decrease in low-level Z_{MRR} from SB to UP is twice as large. The main explanation is an increase in aggregate size from SB to UP, resulting in an increasingly large fraction of particles >3.2 mm in size (Mie scattering threshold at K band) from the shore to the Tug. This is evident in the dramatic increase in $DWR_{S,K}$ (the difference between Z_{KTYX} and Z_{MRR}) from SB (−1.2 dB), via SC (+2.1 dB) and NR (4.8 dB) to UP (7.3 dB) (Fig. 19b). These are average $DWR_{S,K}$ values in the lowest 1 km with data at the respective stations. Similarly, both the $DWR_{K,W}$ and the $DWR_{X,K}$ (Z_{XPR}–Z_{MRR}) values are rather large above SC (~12 and ~7 dB, respectively, in the lowest 1 km with data, Fig. 19b). As mentioned in section 2f, large values of the $DWR_{K,W}$ can be due either to large aggregates or smaller, heavily rimed particles. Kneifel et al. (2015) have shown that, when $DWR_{Ka,W}$ values are large, the presence of large $DWR_{X,Ka}$ values (5–10 dB) is an indication of aggregates. The Ka frequency is slightly higher than the K frequency used here (36 vs 24 GHz), thus $DWR_{X,K}$ should be lower than $DWR_{X,Ka}$ for the same particle population. Thus, the observed $DWR_{X,K}$ ≈ 7 dB certainly is large compared to observations of aggregates in Kneifel et al. (2015), indicating that large aggregates dominate. And the inland increase in $DWR_{S,K}$, together with the rather low $DWR_{K,W}$ values at NR and UP as compared to those at other locations (Fig. 19b), is an indication of growing snow aggregate sizes, with more numerous Mie scatterers at K band (>3.2 mm) farther inland. All this indicates many large particles at low levels, increasing in size toward the Tug.

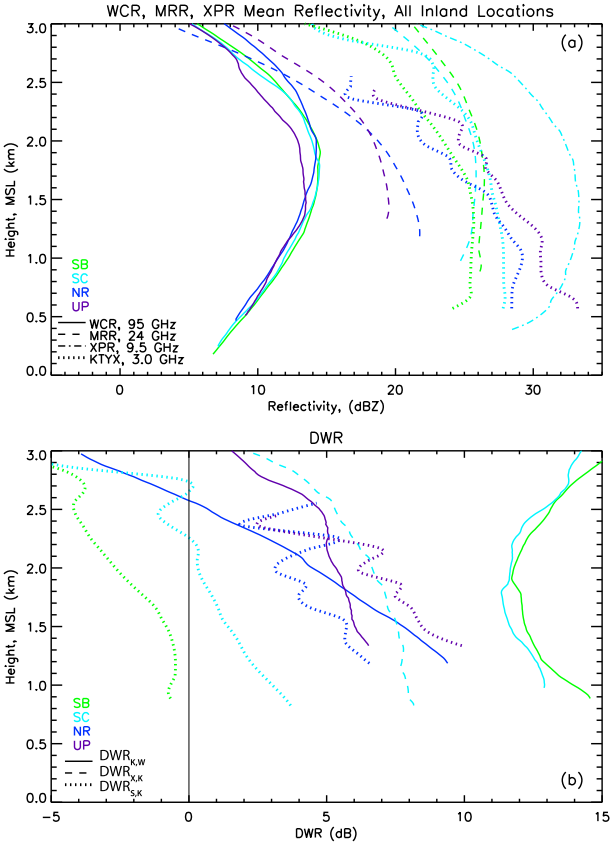

FIG. 19. (a) WCR, MRR, XPR, and KTYX mean reflectivity profiles at the four MRR sites shown in Fig. 2, color coded by location. All values (except WCR) are averaged between 1905 and 2105 UTC. (b) Corresponding profiles of DWR for different pairs of radars.

Much of this snow growth occurs at rather low levels: both the $DWR_{K,W}$ and $DWR_{S,K}$ values generally increase toward the lowest level with data (800 m AGL) (Fig. 19b) and possibly lower. The $DWR_{X,K}$ values also increase toward the ground at SC (below 1.8 km MSL, Fig. 19b). Farther inland, at NR and UP, $DWR_{K,W}$ and $DWR_{S,K}$ values increase most steeply toward the ground suggesting rapid snow growth. This is only possible by aggregation.

7. Conclusions

This paper explores the vertical structure of radar reflectivity and hydrometeor vertical velocity in a well-defined, deep, lake-aligned lake-effect snowband observed on 11 December 2013 over and downwind of Lake Ontario, using four different radar systems from W to S band, complemented by in situ particle observations from an aircraft and on the ground. The purpose is to understand heavy lake-effect snowfall and its intensification over at least some distance inland. We explore two nonexclusive processes that contribute to this: the collapse of convection that lofts hydrometeors over the lake, and stratiform ascent over land attributed to low-level stratification and terrain (the Tug Hill Plateau), leading to more stratiform precipitation there. Expectations for both processes are listed in section 1.

We find that strong convective updrafts and associated BWERs are present offshore, locally producing sometimes heavily rimed snow particles. Consistent with expectations of the collapse of convection, we find values of standard deviation and skewness of vertical velocity decreasing onshore. The echo-top height tends to increase toward the downwind shoreline, but it does not significantly decrease inland, at least not upwind of the Tug.

Consistent with expectations of stratiform ascent, the mean vertical velocity increases inland, and the mean snow diameter increases across the shoreline and over the Tug's foothills, as suggested both by in situ measurements in the air and on the ground, and by differences in reflectivity of radars of different frequency. Low-level snow growth occurs, especially over land and over the Tug, probably due to vapor deposition and aggregation. Multifrequency radar reflectivity and dual-polarization variables consistently indicate the presence of ice crystals aloft and dry aggregates at low levels.

This evidence suggests that both processes contribute to heavy lake-effect snowfall downwind of Lake Ontario: convection lofts some hydrometeors over the water, resulting in rimed particles found locally near BWERs in cloud and at the surface. As the narrow convective updrafts collapse onshore, widespread ascent develops there due to a combination of terrain, low-level stratification, and surface convergence, as shown schematically in Fig. 1. This ascent leads to intense low-level snow growth and heavy stratiform snowfall.

This process description warrants some caution since the conclusions are based on a single case study. A separation of the contribution of each process is impossible from observations alone, and may be the subject of a future modeling study, in which factors such as terrain, surface fluxes, and latent heating can be controlled.

Acknowledgments. This work was funded by the Division of Atmospheric and Geospace Sciences National Science Foundation Grant AGS-1258856. We thank colleagues Binod Pokharel and Yonggang Wang for their assistance in data processing and display. This work also benefitted from data support provided by Ted Letcher, Kevin Knupp, and Dustin Phillips. Additional insight supporting this work was given by Peter Veals. NCAR-EOL maintains the OWLeS data repository from which some data and images were obtained.

REFERENCES

Alcott, T. I., and W. J. Steenburgh, 2013: Orographic influences on a Great Salt Lake–effect snowstorm. *Mon. Wea. Rev.*, **141**, 2432–2450, doi:10.1175/MWR-D-12-00328.1.

Battaglia, A., E. Rustemeier, A. Tokay, U. Blahak, and C. Simmer, 2010: PARSIVEL snow observations: A critical assessment. *J. Atmos. Oceanic Technol.*, **27**, 333–344, doi:10.1175/2009JTECHA1332.1.

Bergmaier, P., B. Geerts, and Y. Wang, 2015: Airborne dual-Doppler observations of the 11 Dec 2013 lake-effect snow band during OWLeS. *16th Conf. on Mesoscale Processes*, Boston, MA, Amer. Meteor. Soc., 8.6. [Available online at https://ams.confex.com/ams/16Meso/webprogram/Paper274239.html.]

Brown, R. A., T. A. Niziol, N. R. Donaldson, P. I. Joe, and V. T. Wood, 2007: Improved detection using negative elevation angles for mountaintop WSR-88Ds. Part III: Simulations of shallow convective activity over and around Lake Ontario. *Wea. Forecasting*, **22**, 839–852, doi:10.1175/WAF1019.1.

Burt, C. C., 2007: *Extreme Weather: A Guide and Record Book*. 2nd ed. W. W. Norton & Company, 303 pp.

Campbell, L. S., W. J. Steenburgh, P. G. Veals, T. W. Letcher, and J. R. Minder, 2016: Lake-effect precipitation enhancement over the Tug Hill Plateau during OWLeS IOP2b. *Mon. Wea. Rev.*, **144**, 1729–1748, doi:10.1175/MWR-D-15-0412.1.

Crewell, S., K. Ebell, U. Löhnert, and D. Turner, 2009: Can liquid water profiles be retrieved from passive microwave zenith observations? *Geophys. Res. Lett.*, **36**, L06803, doi:10.1029/2008GL036934.

Eichenlaub, V. L., 1979: *Weather and Climate of the Great Lakes Region.* University of Notre Dame Press, 335 pp.

Frame, J., D. Conrad, N. Zelasko, C. J. Johnston, and J. Mulholland, 2015: Dual-Doppler observations of boundaries, vortices, and varying band morphology in the long-lake axis parallel snow band of 10-11 December 2013 during the Ontario Winter Lake-effect Systems (OWLeS) Project. *16th Conf. on Mesoscale Processes*, Boston, MA, Amer. Meteor. Soc., 13.3. [Available online at https://ams.confex.com/ams/16Meso/webprogram/Paper274602.html.]

Gaussiat, N., H. Sauvageot, and A. J. Illingworth, 2003: Cloud liquid water and ice content retrieval by multiwavelength radar. *J. Atmos. Oceanic Technol.*, **20**, 1264–1275, doi:10.1175/1520-0426(2003)020<1264:CLWAIC>2.0.CO;2.

Geerts, B., R. Damiani, and S. Haimov, 2006: Finescale vertical structure of a cold front as revealed by airborne radar. *Mon. Wea. Rev.*, **134**, 251–272, doi:10.1175/MWR3056.1.

——, Q. Miao, and Y. Yang, 2011: Boundary layer turbulence and orographic precipitation growth in cold clouds: Evidence from profiling airborne radar data. *J. Atmos. Sci.*, **68**, 2344–2365, doi:10.1175/JAS-D-10-05009.1.

Gourley, J. J., P. Tabary, and J. P. D. Chatelet, 2007: A fuzzy logic algorithm for the separation of precipitating from nonprecipitating echoes using polarimetric radar observations. *J. Atmos. Oceanic Technol.*, **24**, 1439–1451, doi:10.1175/JTECH2035.1.

Hill, J. D., 1971: Snow squalls in the lee of Lakes Erie and Ontario. NOAA Tech. Memo. NWS ER-43, 20 pp.

Hogan, R. J., A. L. M. Grant, A. J. Illingworth, G. N. Pearson, and E. J. O'Connor, 2009: Vertical velocity variance and skewness in clear and cloud-topped boundary layers as revealed by Doppler lidar. *Quart. J. Roy. Meteor. Soc.*, **135**, 635–643, doi:10.1002/qj.413.

Houze, R., Jr., 2014: *Cloud Dynamics.* 2nd ed. Elsevier, 496 pp.

Jing, X., B. Geerts, K. Friedrich, and B. Pokharel, 2015: Dual-polarization radar data analysis of the impact of ground-based glaciogenic seeding on winter orographic clouds. Part I: Mostly stratiform clouds. *J. Appl. Meteor. Climatol.*, **54**, 1944–1969, doi:10.1175/JAMC-D-14-0257.1.

Jiusto, J. E., and M. L. Kaplan, 1972: Snowfall from lake-effect storms. *Mon. Wea. Rev.*, **100**, 62–66, doi:10.1175/1520-0493(1972)100<0062:SFLS>2.3.CO;2.

Klugmann, D., K. Heinsohn, and H.-J. Kirtzel, 1996: A low cost 24 GHz FM-CW Doppler radar rain profiler. *Contrib. Atmos. Phys.*, **69**, 247–253.

Kneifel, S., S. Redl, E. Orlandi, U. Loehnert, M. P. Cadeddu, D. D. Turner, and M.-T. Chen, 2014: Absorption properties of supercooled liquid water between 31 and 225 GHz: Evaluation of absorption models using ground-based observations. *J. Appl. Meteor. Climatol.*, **53**, 1028–1045, doi:10.1175/JAMC-D-13-0214.1.

——, A. von Lerber, J. Tiira, D. Moisseev, P. Kollias, and J. Leinonen, 2015: Observed relations between snowfall microphysics and triple-frequency radar measurements. *J. Geophys. Res. Atmos.*, **120**, 6034–6055, doi:10.1002/2015JD023156.

Kristovich, D. A. R., and R. A. Steve, 1995: A satellite study of cloud-band frequencies over the Great Lakes. *J. Appl. Meteor.*, **34**, 2083–2090, doi:10.1175/1520-0450(1995)034<2083:ASSOCB>2.0.CO;2.

——, and Coauthors, 2016: The Ontario Winter Lake-effect Systems (OWLeS) field campaign: Scientific and educational adventures to further our knowledge and prediction of lake-effect storms. *Bull. Amer. Meteor. Soc.*, in press.

Kumjian, M. R., 2013: Principles and applications of dual-polarization weather radar. Part I: Description of the polarimetric radar variables. *J. Oper. Meteor.*, **1**, 226–242, doi:10.15191/nwajom.2013.0119.

Leinonen, J., and W. Szyrmer, 2015: Radar signature of snow flake riming: A modeling study. *Earth Space Sci.*, **2**, 346–358, doi:10.1002/2015EA000102.

Li, L., and Coauthors, 2001: Retrieval of atmospheric attenuation using combined ground-based and airborne 95-GHz cloud radar measurements. *J. Atmos. Oceanic Technol.*, **18**, 1345–1353, doi:10.1175/1520-0426(2001)018<1345:ROAAUC>2.0.CO;2.

——, G. M. Heymsfield, L. Tian, and P. E. Racette, 2005: Measurements of ocean surface backscattering using an airborne 94-GHz cloud radar—Implications for calibration of airborne and spaceborne W-band radars. *J. Atmos. Oceanic Technol.*, **22**, 1033–1045, doi:10.1175/JTECH1722.1.

Lin, Y., and K. E. Mitchell, 2005: The NCEP Stage II/IV hourly precipitation analyses: Development and applications. *19th Conf. on Hydrology*, San Diego, CA, Amer. Meteor. Soc., 1.2. [Available online at http://ams.confex.com/ams/Annual2005/techprogram/paper_83847.htm.]

Locatelli, J. D., and P. V. Hobbs, 1974: Fall speeds and masses of solid precipitation particles. *J. Geophys. Res.*, **79**, 2185–2197, doi:10.1029/JC079i015p02185.

Maahn, M., and P. Kollias, 2012: Improved Micro Rain Radar snow measurements using Doppler spectra post-processing. *Atmos. Meas. Tech.*, **5**, 2661–2673, doi:10.5194/amt-5-2661-2012.

Markowski, P., and Y. Richardson, 2010: *Mesoscale Meteorology in Midlatitudes.* John Wiley and Sons, 407 pp.

Matrosov, S. Y., 2007: Modeling backscatter properties of snowfall at millimeter wavelengths. *J. Atmos. Sci.*, **64**, 1727–1736, doi:10.1175/JAS3904.1.

——, and A. J. Heymsfield, 2008: Estimating ice content and extinction in precipitating cloud systems from CloudSat radar measurements. *J. Geophys. Res.*, **113**, D00A05, doi:10.1029/2007JD009633.

——, A. Heymsfield, and Z. Wang, 2005: Dual-frequency radar ratio of non-spherical atmospheric hydrometeors. *Geophys. Res. Lett.*, **32**, L13816, doi:10.1029/2005GL023210.

Minder, J. R., T. Letcher, L. Campbell, P. Veals, and J. Steenburgh, 2015: The evolution of lake-effect convection during landfall and orographic uplift as observed by profiling radars. *Mon. Wea. Rev.*, **143**, 4422–4442, doi:10.1175/MWR-D-15-0117.1.

Moyer, A., and G. S. Young, 1991: Observations of vertical velocity skewness within the marine stratocumulus-topped boundary layer. *J. Atmos. Sci.*, **48**, 403–410, doi:10.1175/1520-0469(1991)048<0403:OOVVSW>2.0.CO;2.

Nemarich, J., J. Wellman, and J. Lacombe, 1988: Backscatter and attenuation by falling snow and rain at 96, 140 and 225 GHz. *IEEE Trans. Geosci. Remote Sens.*, **26**, 319–329, doi:10.1109/36.3034.

Niziol, T. A., W. R. Snyder, and J. S. Waldstreicher, 1995: Winter weather forecasting throughout the eastern United States. Part IV: Lake effect snow. *Wea. Forecasting*, **10**, 61–77, doi:10.1175/1520-0434(1995)010<0061:WWFTTE>2.0.CO;2.

Peace, R. L., Jr., and R. B. Sykes Jr., 1966: Mesoscale study of a lake effect snow storm. *Mon. Wea. Rev.*, **94**, 495–507, doi:10.1175/1520-0493(1966)094<0495:MSOALE>2.3.CO;2.

Phillips, D. W., 2009: The UAHuntsville X-Band Profiling Radar (XPR). *34th Conf. on Radar Meteorology*, Williamsburg, VA, Amer. Meteor. Soc., P11.7. [Available online at https://ams.confex.com/ams/34Radar/techprogram/paper_155613.htm.]

Pokharel, B., and G. Vali, 2011: Evaluation of collocated measurements of radar reflectivity and particle sizes in ice clouds. *J. Appl. Meteor. Climatol.*, **50**, 2104–2119, doi:10.1175/JAMC-D-10-05010.1.

Rosenkranz, P. W., 2015: A model for the complex dielectric constant of supercooled liquid water at microwave frequencies. *IEEE Trans. Geosci. Remote Sens.*, **53**, 1387–1393, doi:10.1109/TGRS.2014.2339015.

Steiger, S. M., and Coauthors, 2013: Circulations, bounded weak echo regions, and horizontal vortices observed within long-lake-axis-parallel–lake-effect storms by the Doppler on Wheels. *Mon. Wea. Rev.*, **141**, 2821–2840, doi:10.1175/MWR-D-12-00226.1.

Turner, D. D., S. Kneifel, and M. P. Cadeddu, 2016: An improved liquid water absorption model at microwave frequencies for supercooled liquid water clouds. *J. Atmos. Oceanic Technol.*, **33**, 33–44, doi:10.1175/JTECH-D-15-0074.1.

Tyynelä, J., and V. Chandrasekar, 2014: Characterizing falling snow using multifrequency dual-polarization measurements. *J. Geophys. Res. Atmos.*, **119**, 8268–8283, doi:10.1002/2013JD021369.

Vali, G., and S. Haimov, 2001: Observed extinction by clouds at 95 GHz. *IEEE Trans. Geosci. Remote Sens.*, **39**, 190–193, doi:10.1109/36.898682.

Veals, P., and J. Steenburgh, 2015: Climatological characteristics and orographic enhancement of lake-effect precipitation east of Lake Ontario and over the Tug Hill Plateau. *Mon. Wea. Rev.*, **143**, 3591–3609, doi:10.1175/MWR-D-15-0009.1.

Waldstreicher, J. S., 2002: A foot of snow from a 3000-foot cloud: The ocean-effect snowstorm of 14 January 1999. *Bull. Amer. Meteor. Soc.*, **83**, 19–22, doi:10.1175/1520-0477(2002)083<0019:AFOSFA>2.3.CO;2.

Wang, Z., and Coauthors, 2012: Single aircraft integration of remote sensing and in situ sampling for the study of cloud microphysics and dynamics. *Bull. Amer. Meteor. Soc.*, **93**, 653–668, doi:10.1175/BAMS-D-11-00044.1.

Ware, R., R. Carpenter, J. Guldner, J. Liljegren, T. Nehrkorn, F. Solheim, and F. Vandenberghe, 2003: A multichannel radiometric profiler of temperature, humidity, and cloud water. *Radio Sci.*, **38**, 8079, doi:10.1029/2002RS002856.

White, A. B., P. J. Neiman, F. M. Ralph, D. E. Kingsmill, and P. O. G. Persson, 2003: Coastal orographic rainfall processes observed by radar during the California Land-falling Jets Experiment. *J. Hydrometeor.*, **4**, 264–282, doi:10.1175/1525-7541(2003)4<264:CORPOB>2.0.CO;2.

Wilson, J. W., 1977: The effect of Lake Ontario on precipitation. *Mon. Wea. Rev.*, **105**, 207–214, doi:10.1175/1520-0493(1977)105<0207:EOLOOP>2.0.CO;2.

Young, G. S., D. A. R. Kristovich, M. R. Hjelmfelt, and R. C. Foster, 2002: Rolls, streets, waves, and more: A review of quasi-two-dimensional structures in the atmospheric boundary layer. *Bull. Amer. Meteor. Soc.*, **83**, 997–1001, doi:10.1175/1520-0477(2002)083<0997:RSWAMA>2.3.CO;2.

Yuter, S. E., D. E. Kingsmill, L. B. Nance, and M. Löffler-Mang, 2006: Observations of precipitation size and fall speed characteristics within coexisting rain and wet snow. *J. Appl. Meteor. Climatol.*, **45**, 1450–1464, doi:10.1175/JAM2406.1.